Technical-environmental assessment of rice husk biochars as renewable adsorbents for hydrogen sulphide removal

Process Safety and Environmental Protection 210 (2026) 108688

Contents lists available at ScienceDirect

Process Safety and Environmental Protection

journal homepage: www.journals.elsevier.com/process-safety-and-environmental-protection

Technical-environmental assessment of rice husk biochars as renewable adsorbents for hydrogen sulphide removal

Camilla Galletti [a,1], Francesca Demichelis [a,*,1], Premchand Premchand [b], Debora Fino [a], Raffaele Pirone [a]

[a] Department of Applied Science and Technology (DISAT), Politecnico di Torino,(TO), Corso Duca degli Abruzzi 24, Torino 10129, Italy
[b] Swedish University of Agricultural Sciences, Department of Forest Biomaterials and Technology, 90183 Umea, Sweden

ARTICLE INFO

Keywords:
Biomass
Biochar
Adsorption
Hydrogen sulphide
Life Cycle Assessment

ABSTRACT

This study presents a technical and environmental assessment of H_2S removal using four rice husk (RH)–derived biochars produced by slow pyrolysis. Biochars were obtained under nitrogen (N_2) or carbon dioxide (CO_2) atmospheres, with and without potassium hydroxide (KOH) activation. The investigated materials included unmodified biochars (RH_N_2 and RH_CO_2) and biochars activated before (KOH_RH_CO_2) or after (RH_CO_2_KOH) CO_2-assisted-pyrolysis. Commercial activated carbon (CAC) was used as a reference. Dynamic adsorption experiments were conducted at H_2S concentrations between 35 and 700 ppm and gas hourly space velocities (GHSV) from 3822 to 30,573 h^{-1} . Compared to N_2, CO_2-assisted-pyrolysis enhanced carbon content (74.0 vs. 72.0%), reduced H/C and O/C ratios, and improved specific surface area (SSA) (141.0 vs. 55.7 m^2/g), and micropore volume (0.08 vs. 0.02 cm^3/g). KOH-activation further enhanced SSA (178.4 m^2/g) and micropore volume (0.60 cm^3/g) in pre-activation, while decreasing carbon content due to potassium effects. Among the tested materials, KOH_RH_CO_2 and CAC showed the highest H_2S adsorption capacities. Although KOH_RH_CO_2 exhibited a lower adsorption capacity than CAC at 700 ppm and GHSV of 3822 h^{-1} , it demonstrated superior environmental performance. Life Cycle Assessment results showed that KOH_RH_CO_2 achieved a negative global warming impact, corresponding to approximately 108% of the footprint of CAC but with an opposite sign, effectively shifting the process from carbon-intensive to carbon-negative. This outcome is attributed to the use of agricultural waste as feedstock and to carbon sequestration during CO_2-assisted pyrolysis. Overall, CO_2-pyrolyzed and KOH-activated RH biochars emerge as environmentally advantageous adsorbents for H_2S removal in gas streams.

1. Introduction

Under the EU Green Deal 2019, Europe is mandated to achieve carbon neutrality by 2050. This transition necessitates a strategic shift toward renewable energy and biofuels to decarbonize the energy sector and mitigate reliance on fossil fuels. However, the presence of hydrogen sulphide (H_2S), a toxic, corrosive, and malodorous compound, poses major challenges to biofuel quality, process safety, and the environment.

H_2S originates from the degradation of sulfur-containing compounds in biomass feedstocks and is commonly detected in several biofuel streams, including biogas produced through anaerobic digestion (AD) of organic waste, syngas derived from biomass gasification, and landfill gas. Its concentration strongly depends on feedstock composition and process conditions, ranging from a few tens to several thousand parts per million (ppm, v/v). AD-derived biogas typically contains 10–10,000 ppm of H_2S (Deublein and Steinhauser, 2010), whereas syngas from gasification processes exhibits levels from 100 to 200 ppm (Gupta et al., 2001), and landfill gas concentrations range from 2 to 96.6 ppm (Ko et al., 2015).

From a safety and regulatory perspective, even low concentrations of H_2S require strict control. The World Health Organization has set an atmospheric threshold limit for H_2S of $\leq$ 0.005 ppm, and prolonged exposure in confined environments should not exceed 5 ppm due to the compound's acute toxicity. In industrial contexts, H_2S removal is

* Corresponding author.
E-mail addresses: Camilla.galletti@polito.it (C. Galletti), francesca.demichelis@polito.it (F. Demichelis), premchand.premchand@slu.se (P. Premchand), debora.fino@poliot.it (D. Fino), raffaele.pirone@polito.it (R. Pirone).
[1] Authors equally contributed to the manuscript

https://doi.org/10.1016/j.psep.2026.108688
Received 23 December 2025; Received in revised form 25 February 2026; Accepted 4 March 2026
Available online 6 March 2026

required to mitigate corrosion and ensure compliance with environmental and process-specific standards: $\leq$ 1000 ppm for direct combustion, $\leq$ 16 ppm for transport fuels, and $\leq$ 0.5 ppm for fuel cell applications (Seo et al., 2021). Consequently, the removal of H_2S from gaseous streams remains a persistent technical, economic, and environmental challenge. Consequently, reliable and robust H_2S abatement systems are essential to ensure safe operation, regulatory compliance, and long-term process integrity in bioenergy facilities.

Current H_2S abatement methods include biological, chemical, and physical techniques (Habeeb et al., 2018).

Biological techniques include in-situ oxidation through micro-aeration or microorganisms within digesters (Thiobacillus) (Sackett, 2010), or ex-situ biofilters and bioreactors (Fonseca-Bermúdez et al., 2023). These methods are cost-effective (Skerman et al., 2017) but are often limited by sensitivity to H_2S concentration fluctuations, long residence times, and large spatial requirements (Jiang et al., 2022).

Chemical oxidation using metal (i.e. Fe^{2+}/Fe^{3+}) ions or solid oxidants (i.e. hydrogen peroxide, chlorine, potassium permanganate) offers high removal efficiencies; however, these methods are associated with operational complexity, reagent handling hazards, and secondary environmental impacts (Habeeb et al., 2018).

Physical removal techniques, particularly adsorption, are widely adopted in industrial practice due to their operational flexibility, modularity, and high removal efficiency. While liquid absorption with chemical solvents is effective, it is energy-intensive and capital-demanding (Skerman et al., 2017; Seo et al., 2021). As a result, solid adsorption has emerged as a preferred option for H_2S removal from gas streams. Commercial activated carbon (CAC), metal oxides, or zeolites are adopted. CAC production requires high activation temperatures (400–1100 °C) (Heidarinejad et al., 2020), frequent regeneration needs (Seo et al., 2021), and elevated operating costs (Sahota et al., 2018).

To address these limitations, biochar has emerged as a promising waste-derived adsorbent offering a low-cost and alternative bio-based material for H_2S removal. Biochar is produced via slow pyrolysis of biomass under oxygen-limited conditions (300–700 °C), resulting in lower energy consumption compared to CAC.

Among available biomass feedstocks for biochar production, cereal residues represent nearly 60% of global agricultural waste (Voccia et al., 2025), with rice husk (RH) being one of the most abundant yet underutilized residues. Currently, RH is mainly used as low-value fuel or animal bedding (Calbry-muzyka et al., 2022) (E. Commissions, Agri-food-portal, 2025). RH conversion into biochar aligns with the circular economy targets by enabling waste exploitation and the production of value-added functional materials. Unlike CAC, which exhibits surface areas of 200–2000 m^2/g and pore volumes of 0.1–1 cm^3/g, raw biochar typically requires activation to enhance porosity and adsorption capacity (Shang et al., 2016a).

Previous studies on rice husk (RH)-derived biochar for H_2S removal have largely focused on biochar production under nitrogen atmosphere and chemical activation with strong alkaline agents and/or metal impregnation to enhance adsorption capacity (Chen et al., 2020). Aggressive alkali activation may lead to pore blockage and self-ignition (Shang et al., 2016a).

Shang et al. (2016) examined how pyrolysis temperature (ranging from 100 to 500 °C) influenced the surface area and pH of RH-derived biochar for the removal of 50 H_2S (Shang et al., 2016b), without exploring the alkaline activation. Nam et al. (2018) focused on removing H_2S (400 ppm) with the RH-derived biochar pyrolyzed at 450 °C, followed by activation with high alkali concentration (7 M KOH at 750 °C), followed by copper impregnation (16%) (Nam et al., 2018). Furthermore, Seo et al. (2021) investigated the removal of 1000 ppm of H_2S using RH-derived biochar activated with different alkaline agents like NaOH, KOH, Na_2CO_3, and K_2CO_3 across a molarity range of 1–10 M (Seo et al., 2021).

Furthermore, most studies emphasize technical performance, while the environmental implications associated with biochar production and modification remain largely overlooked.

Life Cycle Assessment (LCA) enables systematic evaluation of environmental burdens and process hotspots across material life cycles. Existing LCA studies on biochar as an adsorbent primarily include CO_2 capture (with olive-pomace-derived biochar) (Zhao and Monteagudo, 2026), syngas cleaning (with biochar-metal-catalyst) (Frazier et al., 2015), and contaminant removal from wastewater (uranium adsorption) (Shen and Fu, 2018), as well as broader assessments within circular economy frameworks (Moreira et al., 2017; Carvalho et al., 2022). However, no peer-reviewed study has yet applied LCA to raw or activated biochar engineered for H_2S adsorption in gas streams, leaving critical environmental trade-offs unresolved.

In addition, CO_2-assisted pyrolysis, a promising strategy for tailoring surface chemistry while potentially reducing environmental burdens, has been scarcely explored for H_2S adsorption and has only been reported for limited feedstocks under high pyrolysis temperature (coffee waste biochar at 800 °C) (Nowicki et al., 2014).

To address these technical and environmental gaps, this study evaluates the H_2S adsorption performance of four rice husk (RH)-derived biochars produced under N_2 and CO_2 atmospheres using mild KOH pre- and post-activation strategies, thereby clarifying the combined effects of controlled CO_2 activation and alkaline treatment. Building upon our previous research (Premchand et al., 2024), the present study explored one biochar generated under nitrogen (RH_N_2), while three were prepared under CO_2: unmodified (RH_CO_2), pre-activated with KOH (KOH_RH_CO_2), and post-activated with KOH (RH_CO_2_KOH). A mild activation protocol was adopted, involving a 1:1 KOH-to-biomass mass ratio (pre-pyrolysis) and a 1:1 KOH-to-biochar mass ratio (post--pyrolysis) at room temperature, to minimize ignition risks and reduce environmental and economic burdens, and was already optimized in (Premchand et al., 2024).

The novelty of this study is the integrated dual-focus approach. The first is the technical process feasibility, including investigation of the synergic effect of pyrolysis atmosphere and KOH- activation under pilot-industrial operational conditions in terms of H_2S concentrations (from 35 to 700 ppm) and gas hourly space velocity GHSV (from 30,573 to 3822 h^{-1}). The second approach consists of an environmental assessment for comparing the environmental impact of the production, activation, and use of the selected adsorbent materials through the Life Cycle Assessment (LCA) methodology (ISO 14040–44:2006), complementing the technical evaluation.

By combining material characterization with a systematic study of operating variables and environmental impacts, this work provides a comprehensive framework for the implementation of renewable, waste-derived adsorbents in industrial biofuel upgrading.

2. Materials and methods

2.1. Preparation of adsorbent materials

Five adsorbent materials were tested to adsorb H_2S.

Four of these were biochars selected based on the findings of a previous study (Premchand et al., 2024). These biochars were derived from rice husks (RH), supplied by Ecopack (Piobesi, Italy). The biochars were produced via slow pyrolysis at 600 °C, employing a heating rate of 15 °C/min and a residence time of 60 min in a stainless steel fixed-bed reactor (with *a* mass load of 10 g). The pyrolysis was carried out under two different atmospheres, nitrogen (N_2) and carbon dioxide (CO_2), with a 5 mL/min flow rate, and involved both pre- and post-pyrolysis activation using potassium hydroxide (KOH).

The first biochar was produced under a nitrogen atmosphere (RH_N_2), while the other three were generated under carbon dioxide (CO_2). Specifically, the second biochar was produced under CO_2 (RH_CO_2). The third and fourth biochars were activated with potassium hydroxide (KOH), applied either before pyrolysis on the raw RH (KOH_RH_CO_2) or after biochar production (RH_CO_2_KOH). The

activation process involved treating the materials with KOH in a 1:1 mass ratio (5 g KOH for 5 g of biomass for pre-pyrolysis and 5 g KOH for 5 g biochar for post-pyrolysis) in 40 mL of distilled H_2O for 6 h at room temperature. At the end of (pre-post) activation, the biochar was washed for three rinses with 20 mL of distilled water for each rinse to reach pH values in the range 8–10. The target was below pH 10 for the possible risk of physical blockage of micropores due to stable mineral precipitates (Qu et al., 2021). Attention was given to the adsorbent produced under CO_2 pyrolysis conditions, as it is stated in the literature that a CO_2 atmosphere can improve the physical properties of biochar compared to the one produced under N_2 pyrolysis (Kim et al., 2019). The four biochars were sieved, and pellets of 2 mm size were selected for the adsorption tests. This study used commercial activated carbon (CAC) (Nortex, Sigma-Aldrich, 2 mm) as a reference adsorbent. The CAC was not activated with KOH like RH because the impregnation of alkaline agents (NaOH, KOH, and K_2CO_3) on CAC decreases its specific surface area (Seo et al., 2021), as the impregnating agents adhere to the surface and pores of CAC, blocking the mesopores and micropores (Tsai, 2002). Conversely, alkaline impregnation on biochar from RH increases the surface area from 84 to 1034 m^2/g (Seo et al., 2021).

2.2. H_2S dynamic adsorption tests

The H_2S adsorption capacity was evaluated through dynamic adsorption tests under dry conditions.

The wet condition adsorption is out of the scope of the current research, because this study aimed to identify the best (technically and environmentally) performing among the five studied adsorbents. Further research will further explore the humidity parameter.

The experiments were conducted using a fixed-bed horizontal reactor (10 mm internal diameter) operating under continuous flow conditions, at atmospheric pressure and ambient temperature (25 ± 2 °C). The reactor setup included two valves, positioned at the beginning (inlet) and end (outlet) of the system, to allow bypass operation for system calibration and setting the desired initial H_2S concentration.

The dynamic adsorption tests were performed by varying two key parameters: the H_2S concentration and the gas hourly space velocity (GHSV), defined as the volume of fed gas per unit volume of adsorbent. These parameters were varied to determine the optimal conditions of H_2S capture.

The tested H_2S concentrations were: 700, 350, 175, 70, and 35 ppm. Calibration of H_2S was performed within this range and is reported in Figure S1. A certified gas mixture containing 700 ppm of H_2S in N_2 (SIAD, Italy) was used as the source of gas, and lower concentrations were obtained by dilution with pure dry N_2.

During the experiment, the gas stream (from the H_2S/N_2 and N_2 cylinders) entering the reactor was maintained at a constant flow rate of 200 mL/min using a mass flow controller system (Brooks, USA). The tested GHSVs were 30,573 h^{-1} , 15,286. h^{-1} , 7463 h^{-1} , and 3822 h^{-1} . These GSHVs were selected based on a review of scientific literature, which reports values ranging from as high as 26,098 h^{-1} (Seo et al., 2021) and 5971.3 h^{-1} (Yuan et al., 2021), to as low as 63.9 h^{-1} (Choudhury and Lansing, 2021), and they were further refined to suit the specific experimental constraints of the laboratory setup (reactor geometry and flow rate).

Experimentally, the GHSV was modulated by varying the reactor bed height and the corresponding mass of adsorbent, while maintaining a constant total flow rate of 200 mL/min (12 L/h). Specifically, bed heights of 0.5, 1.0, 2.0, and 4.0 cm (utilizing around 0.1, 0.2, 0.4, and 0.6 g of adsorbent, respectively, to fill the volume) correspond to GHSVs of 30,573, 15,286, 7643, and 3822 h^{-1} .The adsorption tests were divided into two experimental phases.

The first phase was a screening to evaluate and compare the H_2S removal performance of the five adsorbents to identify materials with the highest adsorption capacity, which were then investigated in depth in the next step. Tests were conducted at two inlet H_2S concentrations (35 and 70 ppm) and three GHSV values (30,573, 15,286, and 7463 h^{-1}).

The second phase involved optimization and validation, focusing on the two adsorbents with the highest H_2S removal efficiency from the screening phase. The second phase aimed to identify the operating conditions that maximize H_2S capture efficiency, enhance adsorption capacity per unit mass, and extend the breakthrough time. Tests were performed across the full H_2S concentration range (35–700 ppm), using two GHSV values: 7463 h^{-1} (to ensure consistency with the screening phase) and 3822 h^{-1} (to assess the effect of extended gas-solid contact time on adsorption performance). This concentration range reflects typical H_2S levels found in biogas (Deublein and Steinhauser, 2010) and biofuels as syngas (Gupta et al., 2001).

The H_2S outlet concentration was monitored at 2-minute intervals with a gas chromatograph (Micro GC Fusion® Gas Analyzer) equipped with a detector column for H_2S. In each test, the exhaust gas of H_2S was absorbed with a NaOH solution of 1.0 M. The reactor operated until the H_2S outlet concentration was equal to the inlet concentration.

2.3. Evaluation of the efficiency of adsorption tests

The breakthrough time and adsorption capacity quantified the performance of the adsorbent materials. Breakthrough time quantifies the efficiency of adsorbent material, representing the time required for the H_2S concentration in the outlet gas stream to reach a predefined threshold (typically 5% of the inlet concentration). It identifies the point at which the adsorbent loses effectiveness, allowing H_2S to pass through the adsorption bed. A longer breakthrough time indicates greater H_2S retention capacity, reflecting higher adsorption performance.

H_2S adsorption capacity measures the total amount of H_2S adsorbed until the outlet concentration equals the inlet concentration, by representing the maximum adsorption per unit weight of the adsorbent. It is determined from the breakthrough curve obtained during adsorption testing.

The adsorption capacities $Q_{removed}$ (in mg of H_2S removed/g of char) were calculated through Eq. (1):

$$Q_{removed} = \frac{Q_v \bullet MW \bullet C_0}{m \bullet V_M} \bullet \int_o^{t_s} (1 - \frac{C(t)}{C_0}) dt \quad (1)$$

where Q is the H_2S removal capacity of adsorbent (mg/g), Q_v is the gas flow rate (mL/min), m the amount of adsorbent (g), MW the mole mass of H_2S (34.08 mg/mmol), V_M the molar volume of gas (22.4 mL/mmol at room temperature), C_0 the inlet level of H_2S (ppm), C(t) the outlet level of H_2S (ppm) and t_s is the adsorption saturation time (min).

2.4. Characterizations of fresh and spent adsorption materials

Chemical and physical characterisations were performed on fresh and spent adsorption materials to compare their properties and to evaluate their adsorption capacity.

Proximate and ultimate analyses were performed through thermogravimetric analysis (TGA/SDTA851e, Mettler Toledo, Columbus, USA) according to ASTM D7582–15. Moisture content (MC) was evaluated by heating 10–12 mg of sample from ambient temperature to 105 °C at a rate of 10 °C/min, followed by a 5 min hold at 105 °C. The temperature was then increased to 900 °C at a rate of 15 °C /min and held for 7 min to eliminate volatile matter (VM). The ash content was determined by slowly heating a dried sample at 600 °C in an air atmosphere for 2 h. The fixed carbon (FC) content was calculated as shown in Eq. (2):

$$FC\ (\%) = 100 - MC\ (\%) - VM\ (\%) - ash \quad (\%) \quad (2)$$

The carbon (C), nitrogen (N), hydrogen (H), and sulfur (S) contents of the adsorption materials were determined using a CHNS analyzer (Elemental Cube, Germany) via combustion at 950 °C, and the weight percentage of oxygen was calculated by difference, considering the ash

content. The surface area and total pore volume were evaluated using the N_2 adsorption method on a BET analyser (Micromeritics TriStar II 3020). Before BET analysis, the degassing of samples was carried out under vacuum for 2 h at 300 °C. The samples were then cooled in a liquid nitrogen bath at −196 °C for the analysis. The surface morphology was evaluated with a field-emission scanning electron microscope (FESEM; Zeiss Merlin, Germany). The samples were placed on a carbon tape, subjected to a platinum coating, and observed under different magnifications with an acceleration voltage of 5 kV. The microscope is equipped with an energy-dispersive X-ray detector (X-ACT EDS, Oxford Instrument, UK) able to perform a fully quantitative analysis of elements present in the samples. The pH was measured by using the pH meter (PH50 XS+DHS, GEASS S.r.L.) by dissolving 1 g of the adsorption material sample in the distilled water with a ratio of 1:40 (biochar: distilled water), stirred for 10 min at 100 rpm, and equilibrated for 30 min (Izhar et al., 2022). The filtered water was used for ICP-MS analysis performed with Thermo Fischer ICAPQ, aimed at quantifying the sulphur content released, detecting it as elemental sulphur.

2.5. Environmental evaluation

Environmental evaluation was performed with Life Cycle Assessment (LCA) methodology according to ISO 14040–44:2006 and divided into four phases: goal and scope, life cycle inventory, life cycle impact assessment, and results and interpretation. The LCA analysis was performed with the software SimaPro 9.05 and the database Ecoinvent 3.5.

In this paragraph, the methodological LCA assumption is described, but the inventory data will be provided in the results section according to the experimental results obtained in paragraph 3.3.

The goal of the study was to compare the environmental impacts of CAC (considered as reference adsorbent material) and the most performing RH-derived biochar under the highest H_2S concentration and GHSV identified in paragraph 3.3.

The functional unit (FU) is the reference to which all environmental impacts are quantified, ensuring consistency with the study's goal. In this work, the FU is defined as the total mass (mg) of H_2S removed, based on the best performance of the most efficient adsorbent identified in Section 3.3. The selection of the mass of pollutant removed as the FU aligns with established practices in LCA studies for gas and liquid-phase adsorption (Frazier et al., 2015; Ho et al., 2025).

The system boundary was considered from a grave-to-gate. This framework was adopted because the rice husk (RH) is a by-product derived from the initial biomass (the grave), and the process endpoint is defined by the adsorption of H_2S (the gate).

The system included a foreground system and a background system in agreement with (Clift et al., 2000). The foreground system is directly involved with the reference flow management, and the background system is linked with the foreground system, including energy production, chemical supply, and avoided products (Thushari et al., 2020).

The study is conducted in Italy, and to ensure the representativeness of the Life Cycle Inventory (LCI), the Italian energy mix and Italian resources were considered in the Ecoinvent database. The specific flows, including their origin and the modelling of individual processes, are reported in the Supporting Information (Tables S5-S8).

According to the zero-burden assumption, RH was assumed as a zero-burden since it did not contain any credits related to the impacts produced during its previous stages of life cycle (Buttol et al., 2007), but only the one related to the transport to the treatment plant.

Multi-output products have been managed considering system expansion by expanding the boundaries of the system to include the avoided primary production by the recovery of materials and energy from pyrolysis. According to ISO 14040–44:2006, system expansion is preferred over allocation to manage multi-output products. A consequential approach was adopted according to (Pereira et al., 2024).

The environmental impacts were calculated with ReCiPe MidPoint (H) 2016 to provide an overview of environmental impacts among the impact categories between CAC and RH-derived biochar. To verify result consistency across a broader range, the sensitivity analysis was performed by increasing the H_2S concentration while maintaining the original GHSV of the original LCA analysis.

3. Results

3.1. Characterization of adsorbent materials

This study investigates five adsorbent materials for H_2S adsorption tests: RH_N_2, RH_CO_2, KOH_RH_CO_2, RH_CO_2_KOH, and CAC as a reference. Table 1 presents the elemental composition, pH, and metal content of the samples to investigate how these physicochemical properties may influence H_2S removal efficiency.

The chemical and physical properties of the samples were analyzed by first examining the influence of the pyrolysis atmosphere (N_2 vs. CO_2), followed by the effects of KOH treatment (pre- and post-activation).

Regarding the pyrolysis atmosphere, CO_2 increased the carbon content of the biochars (from 72.0% to 74.0%) while decreasing hydrogen (from 2.3% to 2.09%) and oxygen (from 5.97% to 3.03%) contents, compared to the N_2 atmosphere. CO_2 promotes carbonization by reducing hydrogen and oxygen through reactions that suppress secondary processes, preventing their retention (Kim et al., 2021). As a result, biochars produced under CO_2 show lower H/C and O/C ratios compared to those produced under N_2, reflecting a higher degree of aromaticity and enhanced thermal stability (Kim et al., 2021) (Yi et al., 2022). In terms of proximate analysis, the biochar produced under CO_2 (RH_CO_2) exhibited lower volatile matter and higher ash content compared to RH_N_2. This can be attributed to the role of CO_2 as a diluent gas, which reduces the volatility of organic compounds by favouring their conversion into more stable carbonaceous structures. Then, the higher fixed carbon (FC) content under CO_2 conditions likely results from the transformation of labile carbon into more stable forms, further contributing to the carbonization process (Liu et al., 2018). Regarding ash content, it is correlated to pH, as it primarily consists of inorganic mineral constituents (Wani et al., 2020). The elevated ash content in RH_CO_2 corresponded to a higher pH value than that of RH_N_2. Pyrolysis in a CO_2 atmosphere may promote specific chemical transformations that modify the inorganic composition of biochar, thereby influencing its pH (Aktar et al., 2022).Concerning specific surface area (SSA) and pore volume (PV), CO_2-assisted pyrolysis resulted in higher values compared to those obtained with pyrolysis in N_2 (141.0 vs. 55.7 m^2/g for SSA and 0.084 vs. 0.018 cm^3/g for PV). This observation is consistent with studies on other feedstocks, such as biosolids (Aktar et al., 2022), where CO_2 enhanced the porosity and surface area of the produced biochars. One proposed mechanism is that CO_2 alters the pyrolysis reaction pathways and kinetics, promoting the breakdown of organic matter and facilitating the formation of smaller carbonaceous fragments, which boost the development of porous structures. Metal analysis indicated that RH_N_2 and RH_CO_2 biochars were composed of silicon (9.86–10.63%), mainly due to the composition of the RH feedstock, followed by calcium, potassium, and magnesium, with minimal differences between the pyrolysis atmospheres. Pre-activation with KOH reduced the carbon content, due to KOH reacting with RH carbon (Chen et al., 2020), and increased oxygen content by introducing oxygen-containing functional groups. Pre-pyrolysis KOH activation significantly reduced silicium content (from 10.63% to 0.88%), maybe due to alkali-induced leaching and silica dissolution (Khoshnood Motlagh et al., 2021). However, KOH_RH_CO_2 biochar retained a high potassium concentration (9.95%), possibly due to residual inorganic salts or stable potassium compounds like K_2CO_3 that persisted after pyrolysis and washing (Khoshnood Motlagh et al., 2021).

Post-pyrolysis KOH activation also modified biochar composition but slightly less than pre-activation, since lower exposure to high temperatures limited activation efficiency (Zhao et al., 2022). The reduction in

Table 1
Physicochemical characteristics of rice husk, RH_N_2, RH_CO_2, KOH_RH_CO_2, RH_CO_2_KOH, and CAC.

		RH	RH_ N_2	RH_CO_2	KOH_RH_CO_2	RH_CO_2_KOH	CAC
Biochar yield	(%)	/	31.21 ± 2.23	32.12 ± 2.08	36.46 ± 3.25	32.74 ± 2.22	/
pH	(-)	7.8 ± 0.07	8.84 ± 0.02	9.68 ± 0.01	8.99 ± 0.03	8.02 ± 0.02	8.15 ± 0.02
Carbon	(%)	42.99 ± 2.96	72.00 ± 2.14	74.09 ± 2.08	63.11 ± 1.05	71.08 ± 2.96	71.7 ± 1.34
Hydrogen	(%)	1.79 ± 0.16	2.30 ± 0.11	2.09 ± 0.13	2.17 ± 0.02	2.64 ± 0.33	5.1 ± 0.22
Nitrogen	(%)	3.09 ± 0.03	1.68 ± 0.07	1.68 ± 0.18	0.57 ± 0.16	1.51 ± 0.23	1.71 ± 0.14
Sulphur	(%)	0.35 ± 0.003	0.12 ± 0.001	0.11 ± 0.002	0.06 ± 0.001	0.02 ± 0.002	0.43 ± 0.006
Oxygen[a]	(%)	37.75 ± 3.3	5.97 ± 0.14	3.03 ± 0.09	7.29 ± 0.16	5.5 ± 0.99	3.19 ± 1.28
H/C	(mol/mol)	0.50 ± 0.003	0.383 ± 0.001	0.339 ± 0.002	0.413 ± 0.002	0.446 ± 0.002	0.519 ± 0.001
O/C	(mol/mol)	1.121 ± 0.001	13.706 ± 2.12	13.788 ± 1.01	6.493 ± 1.21	11.716 ± 1.71	8.273 ± 0.23
VM	(%)	54.15 ± 5.26	15.3 ± 1.24	14.09 ± 2.09	13.4 ± 1.99	13.1 ± 2.31	2.04 ± 0.001
Ashes	(%)	14.04 ± 2.12	18.2 ± 1.56	19 ± 2.65	26.8 ± 3.13	20.2 ± 1.52	19.87 ± 1.41
Moisture	(%)	0.48 ± 0.004	0.22 ± 0.001	0.21 ± 0.003	0.19 ± 0.001	0.54 ± 0.003	3.1 ± 0.01
FC	(%)	31.33 ± 2.98	66.28 ± 4.53	67.39 ± 3.22	59.61 ± 2.01	66.16 ± 3.11	73.90 ± 4.01
SSA	(m^2/g)	nm	55.7 ± 1.02	141.0 ± 1.03	178.4 ± 0.85	152.0 ± 0.69	1459.9 ± 0.12
V micro-pore	(cm^3/g)	nm	0.018 ± 0.001	0.084 ± 0.002	0.598 ± 0.004	0.311 ± 0.002	0.787 ± 0.001
Si	(%)	nm	9.86 ± 0.32	10.63 ± 1.05	0.88 ± 0.21	3.02 ± 0.20	3.63 ± 1.23
Ca	(%)	nm	0.13 ± 0.02	0.19 ± 0.08	nd	0.49 ± 0.02	0.09 ± 0.009
Mg	(%)	nm	0.18 ± 0.01	0.14 ± 0.05	0.10 ± 0.01	0.15 ± 0.06	01.0 ± 0.07
K	(%)	nm	0.63 ± 0.23	0.61 ± 0.13	9.95 ± 2.30	1.14 ± 0.10	0.81 ± 0.05
Na	(%)	nm	nd	nd	nd	nd	nd
S	(%)	nm	0.12 ± 0.001	0.11 ± 0.002	0.006 ± 0.001	0.02 ± 0.002	0.43 ± 0.006
P	(%)	nm	nd	nd	nd	nd	nd

*nm = not measured. BET surface area and pore volume analyses were not conducted for raw rice husk due to its unsuitable shape and size for the measurement setup.
**nd= non-detected

carbon content may be attributed to KOH-induced erosion (Chen et al., 2020) or the removal of soluble organic carbon during washing (Zhao et al., 2022). The significant increase in oxygen content suggests the formation or stabilization of oxygen-containing functional groups, enhancing biochar hydrophilicity. Post-pyrolysis KOH activation also minimized silicium content (1.6%) due to alkali leaching, and RH_CO_2_KOH biochar showed a lower potassium concentration (1.14%), indicating successful removal of residual inorganic salts through washing.

All biochars were alkaline, with pH values ranging from 8.2 to 8.9. Pyrolysis under a CO_2 atmosphere produced biochar with a higher specific surface area (141.0 m^2/g) and micropore volume (0.08 cm^3/g) compared to pyrolysis under N_2 (55.7 m^2/g and 0.02 cm^3/g, respectively), consistent with literature (Premchand and Aqsha, 2023). KOH activation further improved these properties: KOH_RH_CO_2 exhibited a surface area of 178.4 m^2/g and a micropore volume of 0.60 cm^3 /g, while RH_CO_2_KOH reached 152.0 m^2/g and 0.311 cm^3 /g. These enhancements can be attributed to KOH-induced pore formation and volatile removal, with CO_2 amplifying these effects by modifying biomass thermal degradation pathways (Nguyen et al., 2021; Lee et al., 2017).

FESEM analysis was performed, as reported in Fig. 1, to observe the morphological structure of the adsorbent materials. This revealed that pyrolysis did not alter the RH structure, though CO_2 favoured the formation of more circular and uniformly distributed pores. KOH pretreatment increased pore size, as reflected in the order-of-magnitude increase in pore volume (Table 1), maybe due to enhanced removal of volatile organic matter. KOH activation also facilitated carbon etching and oxygenated species reactions, promoting additional porosity and gas release.

Thermo-gravimetric analysis was adopted to evaluate the thermal stability of the investigated biochars. It is important to point out that limitations in the interpretation can occur due to overlapping decomposition steps and possible contributions from residual K salts.

Thermal stability analysis (Figure S2) revealed that untreated biochars (RH_N_2 and RH_CO_2) exhibited minimal weight loss up to 400 °C, indicating that most volatiles had been removed before treatment. From 400–800 °C, weight loss occurred, with RH_N_2 losing 7% and RH_CO_2 losing 5% of their initial weight, suggesting that CO_2 pyrolysis enhances fixed carbon content and reduces volatile fractions, thereby increasing thermal stability (Premchand et al., 2023).

Among all materials, KOH_RH_CO_2 was the least thermally stable, losing ~50% of its weight at 800 °C. This instability may be attributed to its low fixed carbon content (59.61% ± 2.01%) and overall carbon content, as resulting from KOH-induced decarboxylation reactions that reduce carbon levels while increasing porosity. Pre-activation of biomass with KOH (KOH_RH) promotes the formation of a porous structure with a high surface area during pyrolysis. While this structure is important for applications like adsorption, it can also make biochar easier to oxidize at high temperatures (Chen et al., 2020). The porosity allows oxygen to penetrate the surfaces of the material, facilitating combustion reactions. Moreover, raw biomass (RH) contains compounds like hemicellulose and lignin, which can form a protective layer on the biochar surface during pyrolysis (Khoshnood Motlagh et al., 2021). However, KOH treatment tends to remove or alter these protective compounds, increasing the biochar's vulnerability to oxidation. Additionally, KOH may introduce inorganic compounds into the biochar, some of which (like potassium) can act as catalysts for oxidation reactions (Chen et al., 2020).

3.2. *Adsorption screening tests of H_2S*

H_2S adsorption screening tests were conducted on RH_N_2, RH_CO_2, KOH_RH_CO_2, RH_CO_2_KOH, and CAC at two H_2S concentrations of 35 and 70 ppm and three GHSV: 30573, 15287, and 7643 h^{-1} . The results (Fig. 2) are discussed first concerning the H_2S concentration variation, followed by the effect of GHSV variation, and then the properties of the adsorbent materials and possible adsorption mechanisms.

Considering the H_2S concentration, increasing values from 35 ppm to 70 ppm at constant GHSV, the adsorption capacity and breakthrough time for all five materials decreased. This trend can be attributed to the faster saturation of surface-active sites at higher H_2S concentrations. As more H_2S molecules are present in the gas stream, the adsorption sites become occupied more quickly, leading to a shorter adsorption phase. Considering adsorption sites as surface binding locations, elevated H_2S concentrations accelerate their occupation.

These findings are consistent with literature studies (Cristiano et al., 2020), which demonstrated a decline in breakthrough time and adsorption capacity when H_2S inlet concentration increased from 200 to 500 ppm, showing a 60% drop in breakthrough time and a reduction in adsorption capacity from 2.00 to 0.80 mg H_2S/g. Cristiano et al., 2020

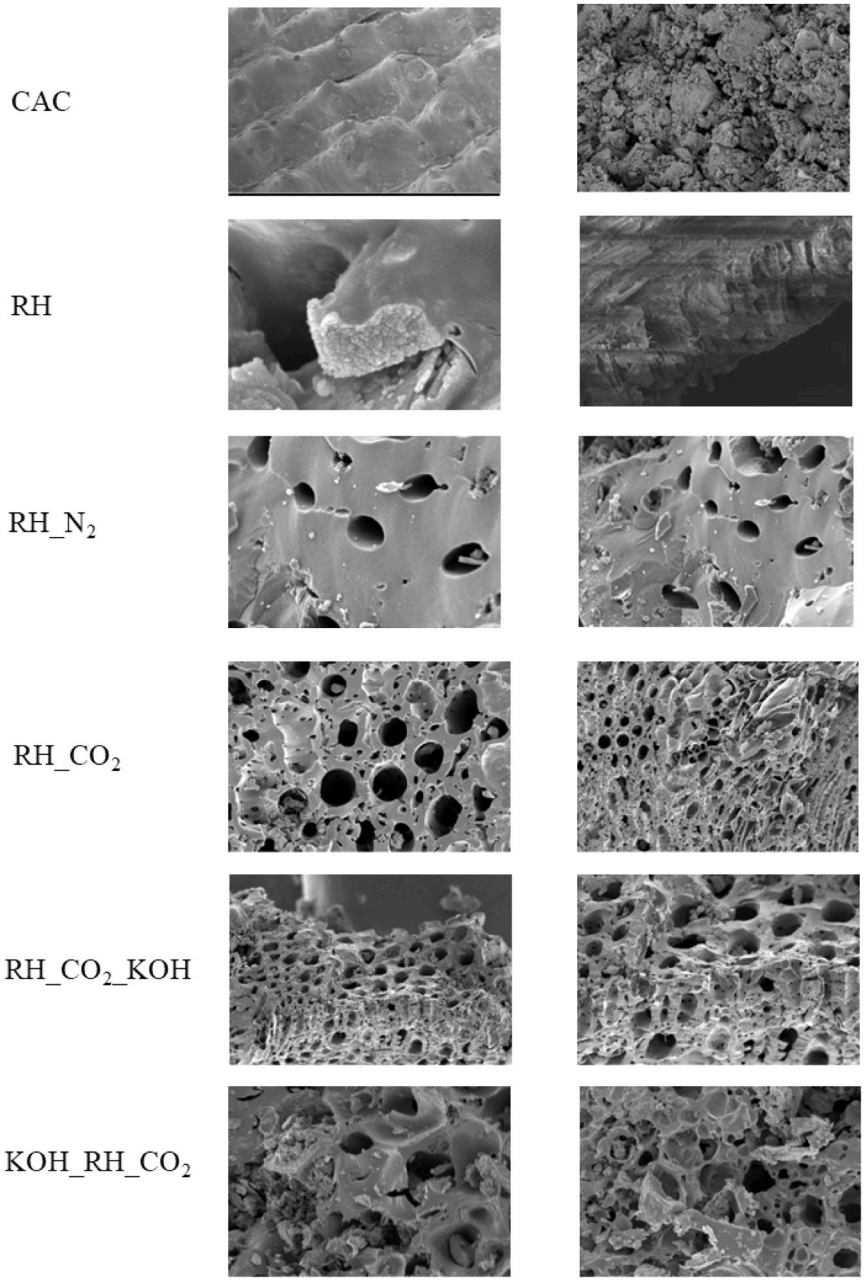

Fig. 1. FESEM analysis: 2 μm scale with 5.00 KX magnification.

(Cristiano et al., 2020) attributed this non-linear decrease to the increase of the mass transfer rate at higher concentration gradients, which can accelerate adsorption site saturation and lower overall performance.

Considering the effect of GHSV, an increase in flow rate from 7643 to 30573 h^{-1} (at constant H_2S concentration) reduced both breakthrough time and adsorption capacity, for all materials. At higher GHSV, the shortened contact time between the gas and the adsorbent bed restricts H_2S diffusion and interaction with the material's micro- and mesoporous structure, resulting in reduced adsorption efficiency. Hence, a high GHSV (30573 h^{-1}) means the gas passes quickly through the adsorbent bed, reducing the contact time. On the contrary, a low GHSV (7643 h^{-1}) significantly increases the contact time, allowing the H_2S to have a longer contact time.

In the test carried out with 35 ppm of H_2S, for example, it was found that reducing the GHSV from 30573 to 7643 h^{-1} increased the adsorption capacity from 1.8 to 44.0 mg H_2S/g for CAC, and from 1.3 to 21.1 mg H_2S/g for KOH_RH_CO_2. This trend aligns with literature studies (Zulkefli et al., 2019) (Saleh, 2018).

It is noteworthy that reducing the GHSV by a factor of approximately four (from 30573 h^{-1} to 7643 h^{-1}) did not result in a proportional four-fold increase in adsorption capacities and breakthrough times (Fig. 3). This finding is consistent with Seo et al. (2021) (Seo et al., 2021), who showed that increasing the height-to-diameter (H/D) ratio from 1 to 4, thus lowering the GHSV, resulted in an eightfold increase in breakthrough time (from 12.32 to 108.56 min). This improvement was attributed to the greater number of active sites available for H_2S to interact with at higher H/D ratios.

Moreover, Cristiano et al. (2020) also observed a non-proportional increase in breakthrough time when decreasing GHSV from 1750 to 1250 h^{-1} (Cristiano et al., 2020).

Therefore, by analysing the H_2S adsorption performance and the physical characteristics of the materials, it can be observed that specific surface area and pore volume are two important factors influencing catalyst activity in the desulphurisation process, as they affect the

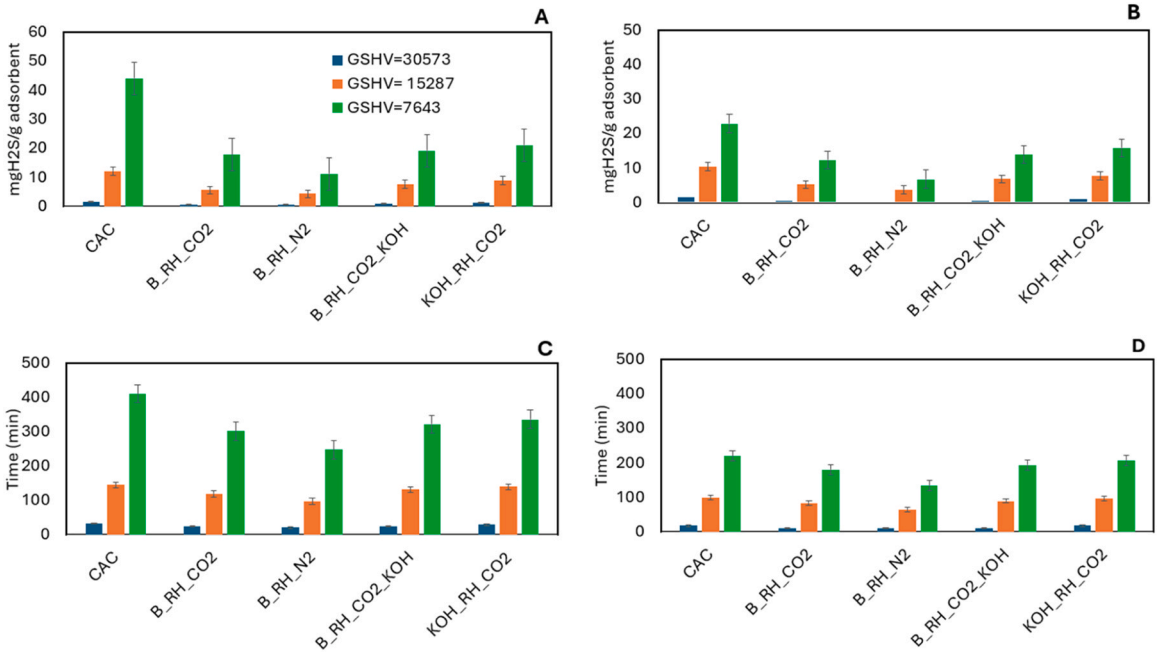

Fig. 2. Adsorption capacity at 35 ppm (A), 70 ppm (B), and breakthrough time at 35 ppm (C), 70 ppm (D) by varying GHSV.

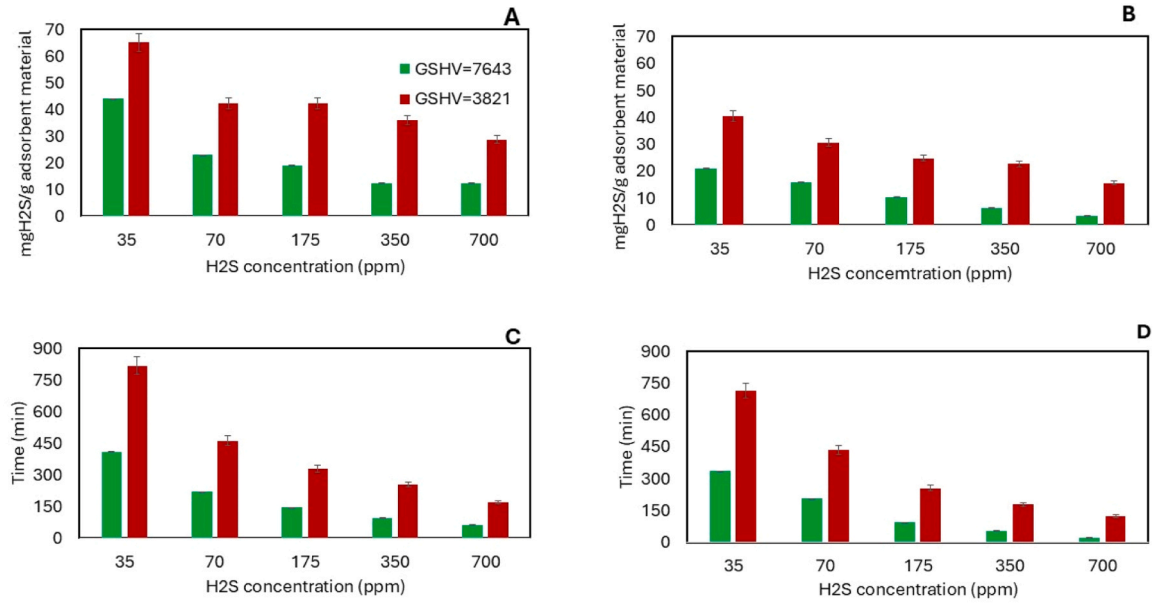

Fig. 3. A) and B) represent the adsorption capacity of CAC and KOH_RH_CO_2, respectively, at gas space hourly velocity (GSHV) of 7463 (green) and 3821 h^{-1}(red). C) and D) represent the breakthrough time of CAC and KOH_RH_CO_2, respectively.

exposure level of the active centre and the sulphur absorption capacity (Surra et al., 2019).

Overall, the best-performing materials were CAC and KOH_RH_CO_2. Despite its lower textural development compared to CAC, KOH_RH_CO_2 exhibited a comparable H_2S removal efficiency, indicating that adsorption performance is governed not only by surface area and porosity but also by surface chemistry and catalytic activity. The H_2S removal behavior of the investigated materials results from a synergistic interplay between physical adsorption, surface alkalinity, and catalytic oxidation. In this context, the performance of KOH_RH_CO_2 is primarily driven by its strong alkaline surface (pH 8.99) and high potassium content (9.95%), the highest among the biochars tested, whereas post-activated RH_CO_2_KOH showed a lower pH (8.02). and potassium content (1.14%). The highly alkaline surface of KOH_RH_CO_2 promotes the dissociative adsorption of acidic H_2S molecules into HS^- and S^{2-} species. Subsequently, potassium species act as effective catalytic centers, facilitating the oxidation of sulfur intermediates into elemental sulfur or sulfate species within the pore network (Yan and Chin, 2004).

Moreover, the elevated ash content of KOH_RH_CO_2 (26.8%), compared to the other tested biochars (18.2–20.2%), provides additional inorganic active sites that further enhance catalytic oxidation pathways. These chemical and catalytic features effectively compensate for the lower specific surface area and porosity of 18.0–20.2% relative to CAC, resulting in a highly reactive adsorbent with an adsorbent capacity comparable to that of the CAC. The superior performance of 18.0–20.2% compared to RH_CO_2, RH_N_2, and RH_CO_2_KOH highlights the

combined role of CO_2-assisted-pyrolysis and KOH pre-activation. CO_2-assisted-pyrolysis enhances carbonization and porosity, while KOH pre-activation introduces strong alkalinity and catalytically active potassium species, yielding an optimized balance between structural and chemical properties for efficient H_2S removal. Deeper kinetics studies will be done in paragraph 3.4

3.3. In-depth study on H_2S adsorption capacity

CAC and KOH_RH_CO_2 exhibited the highest H_2S adsorption capacities during the preliminary screening. Consequently, the second phase of the study focused on a detailed analysis of these two materials, investigating the effect of H_2S concentration and GHSV on their performance.

The in-depth study results (Fig. 3) show the adsorption capacity and breakthrough time for the two materials across a wide H_2S concentration range from 35 to 700 ppm, and at two GHSVs: 7463 h^{-1} and 3822 h^{-1} .

The in-depth investigation assessed the influence of concentration and flow rate on adsorption performance to optimize removal efficiency and extend breakthrough time. Consistent with observations from the screening phase, increasing H_2S concentration significantly decreased the adsorption capacity and shortened the breakthrough time for both materials, regardless of GHSV. This decline is attributed to the faster saturation of active sites at higher inlet concentrations, which shortens breakthrough times (Cristiano et al., 2020). Conversely, decreasing the GHSV substantially increased the gas-adsorbent contact time, thereby improving the performance of both materials.

Considering the combined effect of H_2S concentration and GHSV variations, the reduction in adsorption performance caused by higher H_2S concentration is significantly mitigated by decreasing the GHSV.

Specifically, increasing the H_2S concentration from 35 ppm to 700 ppm, CAC exhibited a capacity reduction of 72% at 7643 h^{-1} and 56% at 3822 h^{-1} , while KOH_RH_CO_2 showed a reduction of 84% and 61% under the same conditions.

Furthermore, reducing the GHSV demonstrated a positive and substantial effect even at the highest H_2S concentration. At 700 ppm, CAC achieved adsorption capacities of 12.4 and 28.7 mg/g with breakthrough times of 62 and 170 min at 7643 and 3822 h^{-1} , respectively. Under the same conditions, KOH_RH_CO_2 reached 3.3 and 15.7 mg/g, with breakthrough times of 22 and 124 min. These results confirm that lower GHSV, enhancing contact time, promotes adsorption and extends breakthrough time, also at the highest concentrations (Cui et al., 2021).

To provide a mechanistic interpretation of these macroscopic performance data, a kinetic study was conducted using the pseudo-first-order kinetic equation (PFO), pseudo-second-order kinetic equation (PSO), and intraparticle diffusion with the Weber-Weber-Morris model (Eqs.3–5) (Table 2).

Unlike the Thomas and Adams–Bohart models, which are primarily used to describe breakthrough curves, the present study adopted pseudo-first-order and pseudo-second-order models to investigate the kinetic nature of dynamic H_2S adsorption on biochars.

These models are essential for elucidating the predominant adsorption mechanism (physical or chemical) that governs the overall removal rate.

The Weber–Morris intraparticle diffusion model was further applied to distinguish the rate-limiting mass transfer mechanisms, providing critical insights into whether the overall kinetics are controlled by boundary-layer resistance or internal pore diffusion. The equations for the pseudo-first-order kinetic and the pseudo-second-order kinetic are linearised according to (Revellame et al., 2020) as follows:

Pseudo first-order kinetic linearised form given by (Revellame et al., 2020)

$$\ln(q_e - q(t)) = \ln q_e - kt \tag{3}$$

Pseudo-second order kinetic linearised form given by (Revellame et al., 2020)

$$\frac{t}{q(t)} = \left(\frac{1}{q_e}\right)t + \frac{1}{k_2 {q_e}^2} \tag{4}$$

Where qe and q(t) (mg g^{-1}) are the amount of H_2S adsorbed at equilibrium and time t (min), k_1 (min^{-1}) and k_2 (g $mg^{-1}min^{-1}$) are the first-order and second-order rate constants, respectively.

The most common practice to determine adsorption kinetic parameters is through the linearized form of the models. This is accomplished by plotting ln (qe – q(t)) vs t for PFO and t $\frac{t}{q(t)}$ vs t for PSO as derived by Eqs. (3) and (4), respectively. The parameters are then estimated from the slope and intercept of the best fit line; if m = slope and b = intercept, k_1 = -m and qe = exp (b) m^{-1} for PFO, while $k_2 = \frac{m^2}{b}$ and qe = $\frac{1}{m}$ for PSO.

The Weber–Morris model identifies the diffusion mechanism, as the previous two models (PFO and PSO) do not apply to the diffusion mechanism. Weber–Morris intraparticle diffusion model is represented by Eq. 5:

Table 2
kinetic studies concerning first and second pseudo-order and the Weber-Morris model considering CAC and KOH-RH-CO_2 at concentration ranges between 35 and 700 ppm under two GSHV 7463 h^{-1} and 3822 h^{-1} .

			Pseudo-first order			Pseudo-second order			Weber-Moris		
		Concentration	k_1 (min^{-1})	qe (mg/g)	R^2	Qe (mg/g)	k_2 (g/mg^{-1} min^{-1})	R^2	k_3	C	R^2
CAC	7463 h^{-1}	35	0.007	0.413	0.785	0.035	0.029	0.989	0.024	-0.121	0.957
		70	0.013	0.408	0.800	0.031	0.074	0.988	0.033	-0.116	0.955
		175	0.020	0.525	0.813	0.027	0.120	0.943	0.051	-0.145	0.951
		350	0.029	0.481	0.828	0.024	0.197	0.958	0.057	-0.127	0.947
		700	0.044	0.707	0.849	0.018	0.729	0.996	0.104	-0.179	0.941
	3822 h^{-1} ,	35	0.004	0.317	0.773	0.069	0.020	0.975	0.013	-0.094	0.959
		70	0.006	0.364	0.783	0.063	0.069	0.955	0.018	-0.107	0.958
		175	0.009	0.504	0.790	0.056	0.094	0.981	0.033	-0.146	0.956
		350	0.011	0.552	0.796	0.049	0.359	0.994	0.041	-0.158	0.955
		700	0.017	0.675	0.808	0.037	0.564	0.997	0.061	-0.189	0.953
KOH-RH-CO_2	7463 h^{-1}	35	0.009	0.246	0.789	0.016	0.034	0.952	0.016	-0.071	0.957
		70	0.014	0.293	0.802	0.014	0.078	0.964	0.024	-0.083	0.954
		175	0.028	0.374	0.827	0.010	0.416	0.997	0.043	0.003	0.948
		350	0.061	0.343	0.867	0.007	0.792	0.984	0.067	-0.105	0.938
		700	0.115	0.115	0.806	0.006	0.805	0.999	0.071	-0.050	0.917
	3822 h^{-1}	35	0.004	0.225	0.775	0.046	0.013	0.900	0.010	-0.066	0.958
		70	0.007	0.276	0.784	0.028	0.059	0.997	0.016	-0.081	0.957
		175	0.011	0.382	0.796	0.026	0.225	0.983	0.028	-0.110	0.955
		350	0.016	0.496	0.807	0.026	0.341	0.984	0.044	-0.139	0.953
		700	0.028	0.539	0.828	0.024	0.429	0.997	0.063	-0.146	0.948

$$q(t) = k_3 \bullet t^{\frac{1}{2}} + C \quad (5)$$

where k_3 is the intraparticle diffusion rate constant (g mg^{-1} min^{-1}), and C is the intercept representing the thickness of the boundary layer. The larger the C value is, the greater the boundary layer effect.

The k_3 and the C were determined as the slope and y-intercept from the linear plot of qt vs $t^{\frac{1}{2}}$, respectively.

The kinetic analysis (Table 2) confirmed that the pseudo-second-order model provided better fits ($R^2 > 0.897$) than the pseudo-first-order model ($R^2 < 0.867$), indicating that the adsorption rate is likely controlled by a chemi-sorption mechanism involving valence forces or electron sharing/transfer. Furthermore, the Weber–Morris model showed the highest correlation ($R^2 > 0.917$), indicating intraparticle diffusion as a key limiting factor.

Under the pseudo-second-order model, an increase in H_2S concentration (from 35 to700 ppm) at constant GHSV was associated with a decrease in the calculated equilibrium adsorption capacity (qe), suggesting that the adsorbent (bed) could not reach its full capacity due to insufficient contact time. This supports the role of intraparticle diffusion as a performance-limiting step, especially at high concentrations, following the literature study (Wang et al., 2019a). The benefit of reducing GHSV is that the higher contact time allows H_2S molecules to diffuse deeper into the porous structure, access internal adsorption sites, and utilize the adsorbent more efficiently. This confirms the critical role of intraparticle diffusion limitations in governing the overall adsorption performance and the non-linear behavior observed (Chiang et al., 2002; Bora et al., 2024). Studies on biochar have shown that the key factors affecting H_2S adsorption include saturation of active sites, pore diffusion, and surface heterogeneity (Wang et al., 2019b). These factors influence adsorption capacity and contribute to non-linear behaviour (Chiang et al., 2002). Additionally, the surfaces of biochar are often heterogeneous, contributing to non-linear concentration dependence (Bora et al., 2024).

KOH_RH_CO_2 exhibited an H_2S removal performance lower but comparable to that of the CAC despite its significantly lower specific surface area (178 vs 1459 m^2/g). This trend can further support that adsorption efficiency is not exclusively ruled by textural properties, but also by surface chemistry and catalytic functionality.

KOH_RH_CO_2 is characterized by a strongly alkaline surface (pH 8.99) and a high potassium content (9.95%) due to KOH activation, which could promote the dissociative adsorption of acidic H_2S molecules into HS^- and S^{2-} species. Potassium species act as catalytic centers, facilitating the oxidation of sulfur intermediates to elemental sulfur or sulfate within the pore network. Additionally, the elevated ash content of KOH_RH_CO_2 (26.8%) provides further inorganic active sites that enhance catalytic oxidation pathways.

Therefore, although KOH_RH_CO_2 possesses a less developed porous structure than CAC, its enhanced surface alkalinity and potassium-driven catalytic activity effectively compensate for the lower surface area.

The performance of KOH_RH_CO_2 aligns with literature trends (Table S3), where H_2S removal efficiency depends on both adsorbent properties (pyrolysis temperature and activation) and operating adsorption conditions (H_2S inlet concentration and GHSV). Literature often focuses on high-temperature pyrolysis and aggressive activation. For instance, Nowicki et al. (2014) (Nowicki et al., 2014) achieved 13.8–20 mg/g (100 H_2S, GHSV 9000) by using coffee-waste biochars with a specific surface area (SSA) of 1000–2000 m^2/g and a process requiring pyrolysis temperature of 500–800 °C and KOH (6 M). In contrast, this study demonstrates that milder conditions (pyrolysis temperature of 600 °C, KOH-biomass 1:1 mass ratio) can yield competitive results. Despite a significantly lower SSA (171 m^2/g), KOH_RH_CO_2 achieved 15 mg/g (175 ppm of H_2S, GHSV 7643 h^{-1}) and 5 mg/g (350 ppm of H_2S, GHSV 7643 h^{-1}).

The synergistic CO_2-assisted pyrolysis and KOH pre-activation compensate for lower porosity by enhancing surface alkalinity and potassium-driven catalytic oxidation. Regarding chemical loading, Cui et al. (2021) (Cui et al., 2021) achieved 22.2 mg/g using high KOH ratios (1:6) at 200 ppm of H_2S and 7000 h^{-1} GHSV. In comparison, our milder activation reached 9 mg/g at 350 ppm of H_2S (GHSV 7643 h^{-1}) but improved to 25 mg/g when the GHSV was reduced to 3821 h^{-1} . This performance is comparable to literature benchmarks, but it proved that optimizing adsorption operating parameters can offset reduced KOH-to-biomass ratios. Ultimately, consistent with Xu et al (Xu et al., 2014). and Seo et al. (2021), the high potassium and ash content in KOH_RH_CO_2 favors dissociative adsorption over purely physical pathways, offering a sustainable, cost-effective alternative to harsher synthesis routes, as the one proposed in (Yuan et al., 2021).

3.4. Characterization of adsorbent materials post-H_2S adsorption

The KOH_RH_CO_2 and CAC samples were characterized after H_2S adsorption conducted at concentrations of 35, 175, and 700 ppm, corresponding to the lowest, intermediate, and highest tested levels, respectively. Adsorption experiments were carried out at a gas hourly space velocity (GHSV) of 3822 h^{-1} , which was identified as the optimal condition for maximum adsorption performance in both materials. In Table 3, the physical properties of the two materials post-H_2S adsorption are reported. A decrease in surface area and pore volume can be observed; in particular, the micropore volume exhibited a marked reduction at the lowest H_2S concentration (35 ppm), whereas the decline in surface area became progressively more significant at higher concentrations (175 and 700 ppm). For CAC, micropore volume decreased by 66.3%, 58.8%, and 48.2% at 35, 175, and 700 ppm of H_2S, respectively, compared to the fresh sample. In contrast, surface area reduction followed the opposite trend, with progressively larger losses of 45.3%, 74.5%, and 86.4%, respectively. KOH_RH_CO_2 exhibited a similar behaviour: micropore volume declined by 64.5%, 47.3%, and 37.8%, while surface area decreased by 30.3%, 57.7%, and 75.5%, across the same concentration range.

This trend suggests that at lower H_2S concentrations, adsorption primarily occurs within micropores, consistent with the high adsorption potential in narrow pores due to overlapping wall effects (Guo et al., 2007). As concentration increases, surface adsorption dominates, limiting diffusion into micropores and resulting in greater surface area loss with less impact on pore volume. These observations align with prior findings for biochar derived from wood waste and municipal solid waste (Hervy et al., 2018).

The reduced micropore accessibility at high H_2S concentrations may also be explained by diffusion limitations, as underlined by the Weber–Morris kinetic model. At higher surface loadings, adsorbed molecules tend to block pore entrances or modify the surface chemistry. This effect is further evidenced by post-adsorption pH variations.

At lower H_2S concentrations, such as 35 ppm, both CAC and KOH_RH_CO_2 show a significant drop in pH after adsorption. The pH values of CAC post adsorption at 35 ppm and 700 ppm were 4.81 ± 0.02 and 6.76 ± 0.02, respectively, while the pH values of KOH_RH_CO_2 post adsorption at 35 ppm and 700 ppm were 5.6 ± 0.03 and 7.2 ± 0.01, respectively.

Moreover, ICP analysis (Table 4) supported the described adsorption mechanisms by quantifying the fraction of adsorbed S that is leached as sulphur from the materials after adsorption. The equipment used could only detect S form without distinguishing among S-species.

Despite higher adsorption capacities at lower H_2S concentrations, the release of sulphur was greater for materials exposed to 700 ppm of H_2S. CAC adsorbed 13482 ppm at a 35 ppm inlet H_2S but released less sulphur than at 700 ppm, where it captured only 2896 ppm. KOH_RH_CO_2 followed the same trend, with 11798 ppm adsorbed at 35 ppm and only 471 ppm at 700 ppm, releasing more sulphur at higher concentration. This result indicates that adsorption at lower concentrations results in stronger retention, likely due to deeper penetration

Table 3
Physical characterization of KOH_RH_CO_2 and CAC before and after H_2S adsorption tests.

		CAC	CAC H_2S= 35 ppm	CAC H_2S= 175 ppm	CAC H_2S= 700 ppm	KOH_RH_CO_2	KOH_RH_CO_2 H_2S= 35 ppm	KOH_RH_CO_2 H_2S= 175 ppm	KOH_RH_CO_2 H_2S= 700 ppm
pH	(-)	8.15 ± 0.02	4.81 ± 0.02	5.2 ± 0.02	4.81 ± 0.02	8.99 ± 0.03	5.6 ± 0.03	6.3 ± 0.02	5.6 ± 0.03 7
Carbon	(%)	71.7 ± 1.34	59.7 ± 1.72	68.7 ± 4.87	70.71 ± 3.28	63.11 ± 1.05	57.61 ± 2.72	55.34 ± 1.94	51.00 ± 2.34
Hydrogen	(%)	5.1 ± 0.22	4.2 ± 0.21	4.2 ± 0.12	4.1 ± 0.33	2.17 ± 0.02	1 ± 0.002	0.98 ± 0.002	0.94 ± 0.002
Nitrogen	(%)	1.71 ± 0.14	1.65 ± 0.002	1.63 ± 0.001	1.6 ± 0.002	0.57 ± 0.16	1.72 ± 0.002	1.7 ± 0.004	1.4 ± 0.001
Sulphur	(%)	0.43 ± 0.006	13.56 ± 2.23	7.67 ± 1.52	2.82 ± 0.99	0.06 ± 0.001	11.81 ± 2.2	2.34 ± 0.72	0.49 ± 0.001
Oxygen[a]	(%)	3.19 ± 1.28	4.24 ± 0.02	1.08 ± 0.004	3.99 ± 0.56	7.29 ± 0.16	8.84 ± 1.29	14.74 ± 2.84	20.07 ± 3.31
H/C	(-)	0.519 ± 0.001	0.844 ± 0.002	0.734 ± 0.007	0.696 ± 0.002	0.413 ± 0.002	0.208 ± 0.008	0.213 ± 0.009	0.221 ± 0.005
O/C	(-)	8.273 ± 0.23	10.560 ± 1.27	47.708 ± 5.78	13.291 ± 2.92	6.493 ± 1.21	4.888 ± 1.92	2.816 ± 0.02	1.906 ± 0.08
VM	(%)	2.04 ± 0.001	8.27 ± 0.02	7.65 ± 0.2	5.22 ± 0.12	13.4 ± 1.99	9.2 ± 1.22	8.78 ± 1.34	7.6 ± 1.98
Ashes	(%)	19.87 ± 1.41	16.65 ± 2.12	16.72 ± 3.32	16.78 ± 3.12	26.8 ± 3.13	19.02 ± 4.82	24.9 ± 2.92	26.1 ± 0.92
Moisture	(%)	3.1 ± 0.01	3.84 ± 0.99	3.86 ± 0.85	3.89 ± 0.72	0.19 ± 0.001	1.9 ± 0.7	1.93 ± 0.09	1.99 ± 0.07
FC	(%)	73.90 ± 4.01	71.24 ± 2.10	71.77 ± 1.13	74.11 ± 3.22	59.61 ± 2.01	69.88 ± 4.42	64.39 ± 5.99	64.31 ± 4.87
Specific surface area	(m^2/g)	1459.899 ± 0.12	769.72 ± 0.32	372.34 ± 0.83	198.049 ± 0.002	178.4 ± 0.85 ± 0.76	124.32 ± 0.92	75.4 ± 0.01	43.67 ± 0.02
V micro-pore	(cm^3/g)	0.787 ± 0.001	0.265 ± 0.020	0.371 ± 0.008	0.407 ± 0.006	0.598 ± 0.004	0.212 ± 0.004	0.315 ± 0.002	0.372 ± 0.002

Table 4
Sulphur releases from CAC and RH-KOH-CO_2 after H_2S adsorption (75, 175, and 700 ppm) at 3821.7 h^{-1}.

	H_2S adsorbed during the tests	S adsorbed during the tests	S dissolved in the liquid *	S on the solid*	Released***
	ppm	ppm	ppm	ppm	%
CA FRESH			43		
CA 35 ppm	14337	13482	346	13136	3
CA 175 ppm	7700	7240	848	6392	11
CA 700 ppm	3080	2896	951	1945	32
RH-KOH-CO_2 FRESH			9		
RH-KOH-CO_2 35 ppm	12546	11798	549	11248	5
RH-KOH-CO_2 175 ppm	2509	2359	280	2079	12
RH-KOH-CO_2 700 ppm	501	471	161	310	34

*measured with ICP
**S on the solid is calculated as the difference between S adsorbed during the test and S dissolved in the liquid, and measured in the liquid.
*** Released is the % ratio between S dissolved in the liquid, and S adsorbed during the test.

into micropores and the formation of more stable physiosorbed interactions.

Overall, the results from Table 3 (physicochemical characterization) and Table 4 (ICP analysis) suggest that at 35 ppm, H_2S release was minimal (2.57% for CAC and 4.66% for KOH_RH_CO_2), indicating that adsorption could be primarily governed by micropore volume. This is supported by the observed reductions in pore volume and specific surface area after exposure to 35 H_2S.

The FTIR spectra (Fig. 4) of KOH_RH_CO_2 and CAC before and after H_2S adsorption reveal the functional groups involved in the removal mechanism. In KOH_RH_CO_2, the fresh material shows bands at ~1700 cm^{-1} (C═O of carboxylic acids), 1450–1380 cm^{-1} (C–H bending), and a strong region at 1200–1000 cm^{-1} attributed to C–O vibrations of alcohols, esters, and ethers. After adsorption, a clear intensification and deformation in the 1150–1000 cm^{-1} region and the appearance of bands assignable to –SO_2 species (≈1350–1150 cm^{-1}) are observed, indicating formation of sulfite/sulfate compounds. These changes confirm dissociative adsorption and subsequent oxidation of H_2S on the alkaline, potassium-rich surface.

CAC exhibits O–H stretching (~3400 cm^{-1}), C═O (~1700 cm^{-1}), aromatic C═C/C–H (~1500–1400 cm^{-1}), and C–O bands (1200–1000 cm^{-1}). After adsorption, spectral modifications appear in the sulfur-related region. Both FTIR of CAC and KOH_RH_CO_2 exhibit a prominent signal in samples exposed to 35 ppm of H_2S, with characteristic peaks. This supports the explanation that low-concentration H_2S exposure leads to more effective and deeper adsorption (which could modify the surface chemical groups).

Furthermore, from the microscopy analyses, FESEM images (Fig. 5) of CAC and KOH_RH_CO_2 before and after H_2S adsorption (35, 175, and 700 ppm), at a space velocity of 3822 h^{-1} , demonstrate surface degradation with increasing H_2S concentration. These morphological changes support the decrease in surface area (Table 3).

Overall, these characterization results align with established adsorption mechanisms. Literature indicates that H_2S removal depends on adsorbent characteristics, such as surface area, pore structure, and surface functionality, as well as operating conditions (H_2S concentration and GHSV) (Surra et al., 2019). Chemical adsorption and oxidation may occur, particularly in materials with surface oxygen functionalities. In

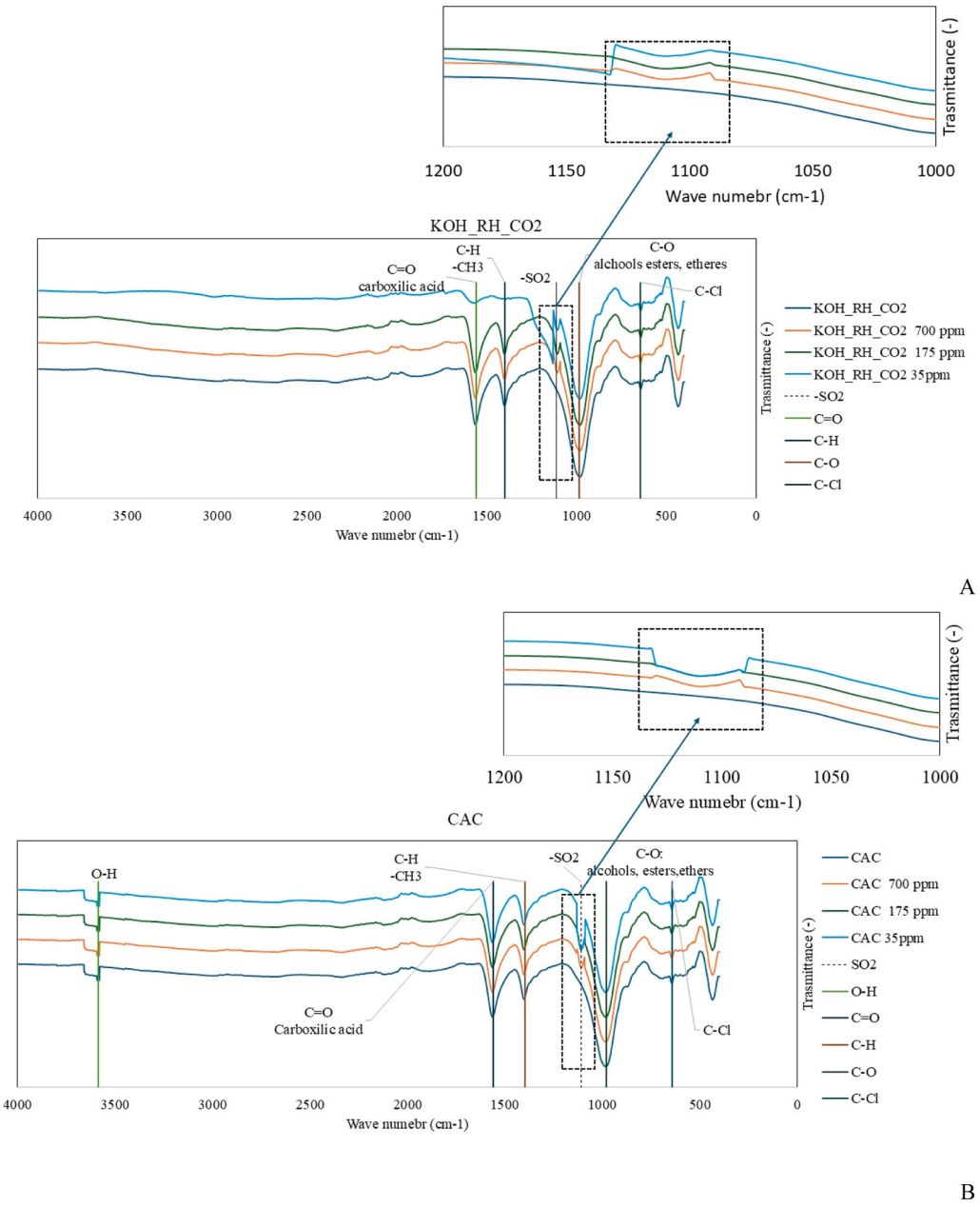

Fig. 4. FTIR spectra of fresh adsorbent material and after adsorption at the GHSV of 3822 h^{-1} with H_2S concentrations equal to 35, 175, and 700 ppm. A) KOH_RH_CO_2 and B) CAC.

this study, KOH_RH_CO_2 had higher oxygen content (7.29%) than CAC (3.19%), potentially enhancing its reactivity despite lower surface area and micropore volume.

Finally, in the absence of oxygen and moisture, physisorption via micropore filling is dominant (Surra et al., 2019). Among the materials tested, CAC and KOH_RH_CO_2 showed the highest micropore volumes and reached the best performance under dry conditions.

It is important to note that even if FTIR evidences sulfur oxides formation on the adsorbent surface, other specific techniques, such as XPS, DRIFTS, or TPD, could be important to be adopted for addressing specific mechanistic questions in future work.

3.5. Environmental analysis

An environmental evaluation was carried out using the Life Cycle Assessment (LCA) methodology (ISO 14040–44:2006). As discussed, in paragraph 3.3, the adsorbent materials exhibiting the highest H_2S removal performance were commercial activated carbon (CAC) and KOH-activated rice-husk biochar pyrolyzed under CO_2 (KOH-RH-CO_2), both tested at a GHSV of 3822 h^{-1} and an inlet H_2S concentration of 35 ppm.

Accordingly, the LCA compared the environmental impacts of the CAC and the KOH-RH-CO_2 biochar systems under the same operational conditions: 35 ppm of H_2S and GHSV = 3822 h^{-1} . The functional unit (FU) was defined as 65 mg of H_2S removed, which corresponds to the maximum adsorption capacity measured for CAC (65 mg H_2S/g CAC) under these conditions. This FU complies with ISO 14040–44:2006 requirements, ensuring consistency with the goal and scope of the study. Inventory data for both the CAC and KOH-RH-CO_2 systems are summarised in Tables S5-S8 and detailed in Section S5. A sensitivity analysis was performed at the same GHSV (3822 h^{-1}) but at a higher inlet concentration (700 ppm of H_2S) to simulate concentration fluctuations

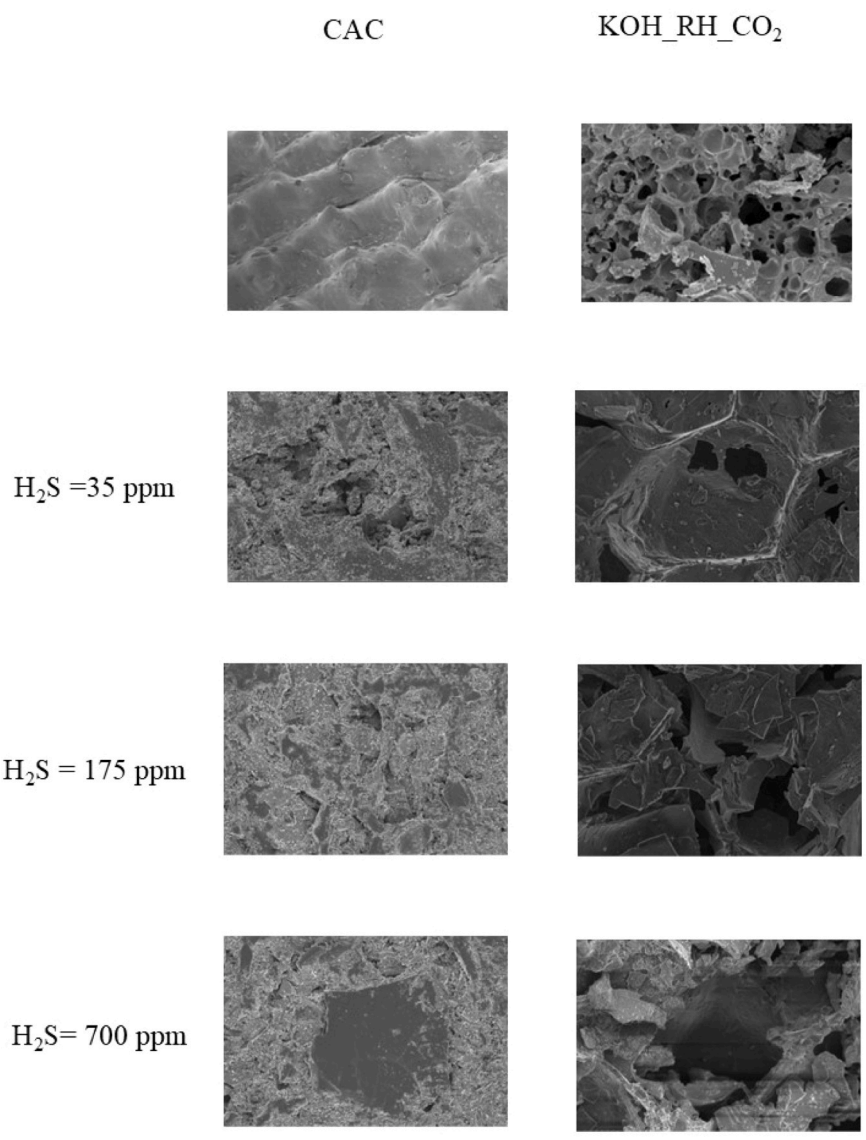

Fig. 5. FESEM analysis on CAC and KOH_RH_CO_2 at GHSV of 3822 h^{-1} with H_2S concentrations of 35, 175, and 700 ppm. 2 μm scale with 5.00 KX magnification.

typical of industrial operation, where gas composition can vary while plant operative conditions like GHSV remain fixed. Under these conditions, H_2S adsorption capacities decreased to 28.72 mg/g for CAC and 15.54 mg/g for KOH-RH-CO_2, enabling verification of the comparative environmental performance across dilute and peak-load scenarios.

The baseline LCA considered the optimal adsorption conditions (35 ppm of H_2S, lowest tested GHSV), whereas the sensitivity scenario represented transient high-load operation. Since low GHSV increases residence time and adsorption efficiency, it extends the adsorbent lifetime and reduces replacement frequency. Consequently, the experimentally identified optimal operating window is directly linked to lower material consumption and improved environmental performance in scaled-up applications.

Environmental impacts were calculated using the ReCiPe MidPoint (H) 2016 method (Table 5).

Although a larger amount of KOH-RH-CO_2 biochar was required to remove the same quantity of H_2S as in the CAC system, the biochar-based configuration exhibits a lower overall environmental impact. This outcome reflects the combined effect of two key parameters: the origin of the biochar and the pyrolysis atmosphere.

First, the biochar derives from an agricultural by-product (rice husks). Its conversion into activated biochar upgrades a waste stream into a functional material and provides avoided burdens associated with waste management. This benefit is especially evident in impact categories such as land use (8.7×10^{-3} vs 1.4 dm^2a crop eq), fossil resource scarcity (-8.7×10^{-2} vs 4.0×10^{-2} g oil eq), and water consumption (-1.2×10^{-2} vs. 1.9×10^{-2} dm^3) compared with CAC.

Secondly, the KOH_RH_CO_2 production was performed under CO_2 in the pyrolysis stage, which can be considered as a carbon capture and storage (CCS) system to mitigate the CO_2 emissions. Consequently, the KOH_RH_CO_2 biochar system showed significantly lower climate-related impacts, with global warming equal to -1.0×10^{-1} g CO_2eq compared to 2.1 g CO_2eq for CAC (which means a reduction of -108%). Similar reductions were observed for stratospheric ozone depletion and ionizing radiation (a reduction of -94%).

Considering the worldwide commitment to achieve climate neutrality by 2050, a focus on climate change is provided in Fig. 6. Regarding global warming, the CAC impacts were dominated by the production of activated carbon itself, reflecting the energy-intensive manufacture and fossil-based precursors typically involved. Conversely, in the KOH-RH-CO_2 system, the activation step represented the main contributor due to chemical consumption; however, partial energy self-sufficiency of the pyrolysis stage compensated for part of these emissions.

Table 5
The environmental evaluation, calculated with ReCiPe MidPoint (H) 2016, compares the impacts of CAC and KOH-RH-CO_2 systems under GSHV of 3822 h^{-1}. The original analysis was conducted at H_2S of 35 ppm, and the sensitivity at H_2S of 700 ppm. The mean and standard deviation include these two H_2S concentrations.

		Mean		Dev.st	
Impact categories	Unit of measure	KOH-RH-CO_2	CAC	KOH-RH-CO_2	CAC
Global warming	g CO_2 eq	-1.0E-01	2.1E+ 00	2.0E-05	4.1E-06
Stratospheric ozone depletion	g CFC11 eq	3.9E-07	6.2E-06	3.6E-11	1.1E-12
Ionizing radiation	Bq Co-60 eq	-7.4E-02	-2.9E-02	5.1E-06	1.3E-06
Ozone formation, Human health	g NOx eq	7.7E-04	3.1E-03	4.9E-08	1.6E-08
Fine particulate matter formation	g PM2.5 eq	7.9E-04	1.6E-03	5.6E-08	1.2E-08
Ozone formation, Terrestrial ecosystems	g NOx eq	7.7E-04	3.9E-03	4.9E-08	1.7E-08
Terrestrial acidification	g SO_2 eq	2.2E-04	1.6E-03	1.6E-09	1.6E-08
Freshwater eutrophication	g P eq	1.7E-04	2.3E-04	1.5E-08	1.0E-10
Marine eutrophication	g N eq	6.6E-06	4.9E-05	6.3E-10	3.3E-11
Terrestrial ecotoxicity	g 1,4-DCB	4.4E+ 00	3.8E+ 00	3.8E-04	8.3E-06
Freshwater ecotoxicity	g 1,4-DCB	3.3E-02	2.4E-02	2.9E-06	1.7E-08
Marine ecotoxicity	g 1,4-DCB	4.4E-02	3.2E-02	3.9E-06	2.5E-08
Human carcinogenic toxicity	g 1,4-DCB	3.6E-02	3.3E-02	3.1E-06	9.7E-08
Human non-carcinogenic toxicity	g 1,4-DCB	7.1E-01	6.0E-01	6.3E-05	8.4E-07
Land use	dm^2a crop eq	8.7E-03	1.4E+ 00	7.0E-07	6.0E-08
Mineral resource scarcity	g Cu eq	3.3E-03	2.3E-03	2.9E-07	1.9E-09
Fossil resource scarcity	g oil eq	-8.7E-02	4.0E-02	8.8E-06	9.0E-07
Water consumption	dm^3	-1.2E-02	1.9E-02	1.0E-06	1.8E-08

Similar trends have been reported in recent LCA of biochar systems, which demonstrate lower climate impacts and resource depletion relative to conventional activated carbons derived from fossil feedstocks (Carvalho et al., 2022; Marzeddu et al., 2021). These results reinforce the suitability of biochar as an alternative adsorbent for industrial gas purification processes under circular-economy and carbon-neutrality frameworks, especially considering that pyrolysis is a mature technology (Technology Readiness Level, TRL, circa 5–6).

4. Conclusions

This study evaluated the technical performance and environmental implications of rice husk (RH)–derived biochars for H_2S removal, produced through pyrolysis under N_2 and CO_2 atmospheres combined with KOH activations. CO_2-assisted pyrolysis enhances carbonization and pore development, while KOH activation improves adsorption capacity through increased microporosity and the introduction of oxygen-containing surface functional groups.

Under low gas hourly space velocity (3822 h^{-1}) and 35 ppm H_2S, the CO_2 pre-activated biochar (KOH_RH_CO_2) exhibited performance comparable to commercial activated carbon (CAC), removing 45 and 65 ppm in 650 and 750 min, respectively. These results demonstrate technical feasibility under low-concentration and contact-time. Post-

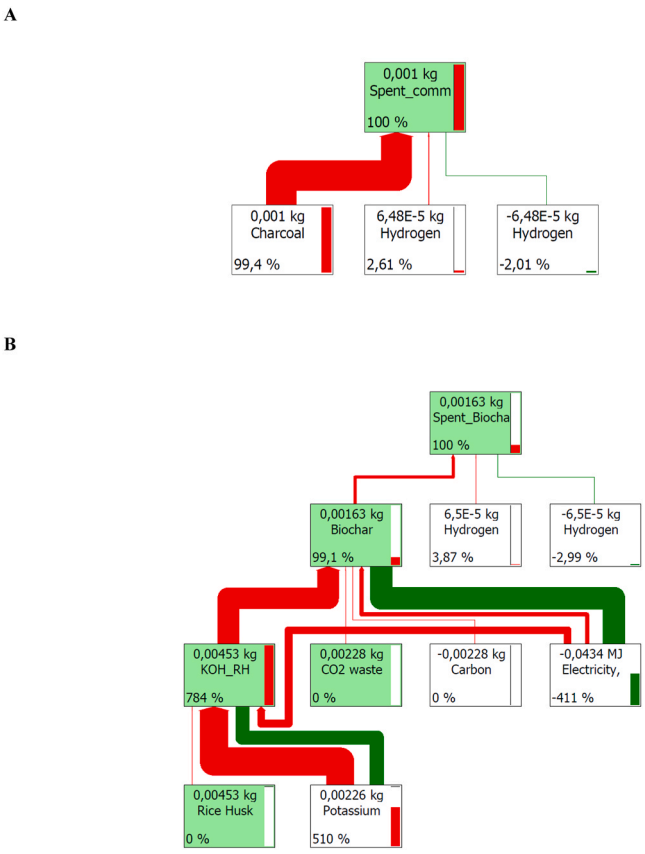

Fig. 6. Sankey diagram expressed in percentage for A) CAC and B) KOH-RH-CO_2 system under GSHV of 3822 h^{-1} and H_2S of 35 ppm.

adsorption analyses revealed a concentration-dependent mechanism: micropore-controlled uptake at low H_2S levels and increasing surface interactions with partial pore blockage at higher loadings, consistent with kinetic and FTIR. Environmentally, KOH_RH_CO_2 exhibited lower impacts than CAC, because the biochar exploited an agricultural by-product by avoiding disposal, and CO_2-assisted pyrolysis represents a carbon capture system. KOH_RH_CO_2 showed a net negative global warming impact, corresponding to -108% of the footprint of CAC; this turns the process from carbon-intensive to carbon-negative. Future works will investigate moisture presence, real biogas composition, cyclic regeneration, temperature effects, and advanced characterization of spent materials and their surface via XPS.

CRediT authorship contribution statement

Camilla Galletti: Writing – original draft, Methodology, Investigation. **Raffaele Pirone:** Writing – review & editing, Supervision, Resources, Project administration, Funding acquisition. **Debora Fino:** Writing – review & editing, Supervision. **Premchand Premchand:** Investigation, Formal analysis. **Francesca Demichelis:** Writing – original draft, Validation, Methodology, Investigation, Formal analysis, Data curation, Conceptualization.

Declaration of Competing Interest

The authors declare that they have no known competing financial interests or personal relationships that could have appeared to influence the work reported in this paper.

Acknowledgment

This paper and related research were carried out as a part of the PON "Ricerca e Innovazione" 2014 – 2020 Avviso MIUR n. 1735 del 13/07/2017 Progetti di Ricerca Industriale e Sviluppo Sperimentale nelle 12 Aree di Specializzazione del PNR 2015-2020. Title of the project: Wet Waste to Green Fuel – Gassificazione rifiuti organici umidi con acqua supercritica per produzione di biometano – GNL. (Acronimus WW-Green-Fuel).

Appendix A. Supporting information

Supplementary data associated with this article can be found in the online version at doi:10.1016/j.psep.2026.108688.

References

Aktar, S., Hossain, M.A., Rathnayake, N., Patel, S., Gasco, G., Mendez, A., de Figueiredo, C., Surapaneni, A., Shah, K., Paz-Ferreiro, J., 2022. Effects of temperature and carrier gas on physico-chemical properties of biochar derived from biosolids. J. Anal. Appl. Pyrolysis 164, 105542. https://doi.org/10.1016/j.jaap.2022.105542.

Bora, D., Roy, K., Mahanta, P., Barbora, L., 2024. Hydrogen sulfide removal from biogas using biomass-derived naturally alkaline biochars: performance analysis and kinetics. J. Mater. Cycles Waste Manag. 26, 1544–1556. https://doi.org/10.1007/s10163-024-01908-8.

Buttol, P., Masoni, P., Bonoli, A., Goldoni, S., Belladonna, V., Cavazzuti, C., 2007. LCA of integrated MSW management systems: case study of the Bologna District. Waste Manag. 27, 1059–1070. https://doi.org/10.1016/j.wasman.2007.02.010.

Calbry-muzyka, A., Madi, H., Rüsch-pfund, F., Gandiglio, M., Biollaz, S., 2022. Biogas composition from agricultural sources and organic fraction of municipal solid waste. Renew. Energy 181, 1000–1007. https://doi.org/10.1016/j.renene.2021.09.100.

Carvalho, J., Nascimento, L., Soares, M., Ribeiro, A., Faria, L., Silva, A., Pacheco, N., Ara, J., Vilarinho, C., 2022. Circ. Econ. Perspect..

Chen, W., Gong, M., Li, K., Xia, M., Chen, Z., Xiao, H., Fang, Y., Chen, Y., Yang, H., Chen, H., 2020. Insight into KOH activation mechanism during biomass pyrolysis: chemical reactions between O-containing groups and KOH. Appl. Energy 278, 115730. https://doi.org/10.1016/j.apenergy.2020.115730.

Chiang, H.L., Tsai, J.H., Chang, G.M., Hsu, Y.C., 2002. Adsorption kinetic characteristics of H2S on activated carbon. Adsorption 8, 325–340. https://doi.org/10.1023/A:1021537530695.

Choudhury, A., Lansing, S., 2021. Journal of environmental chemical engineering adsorption of hydrogen sulfide in biogas using a novel iron-impregnated biochar scrubbing system. J. Environ. Chem. Eng. 9, 104837. https://doi.org/10.1016/j.jece.2020.104837.

Clift, R., Doig, A., Finnveden, G., 2000. The application of life cycle assessment to integrated solid waste management. Part 1 Methodol. Process Saf. Environ. Prot. 78, 279–287. https://doi.org/10.1205/095758200530790.

Cristiano, D.M., de A. Mohedano, R., Nadaleti, W.C., de Castilhos Junior, A.B., Lourenço, V.A., Gonçalves, D.F.H., Filho, P.B., 2020. H2S adsorption on nanostructured iron oxide at room temperature for biogas purification: application of renewable energy. Renew. Energy 154, 151–160. https://doi.org/10.1016/j.renene.2020.02.054.

Cui, S., Zhao, Y., Liu, Y., Huang, R., Pan, J., 2021. Preparation of Straw Porous Biochars by Microwave-Assisted KOH Activation for Removal of Gaseous H2S. Energy Fuels 35, 18592–18603. https://doi.org/10.1021/acs.energyfuels.1c02241.

Deublein, D., Steinhauser, A., 2010. Biogas Waste Renew. Resour. Introd. Second Ed.10.1002/9783527632794.

E. Commissions, Agri-food-portal, Rice (2025). ⟨https://agridata.ec.europa.eu/extensions/DataPortal/rice.html#:~:text=The⟩ EU produces around 2.8,tonnes of milled equivalent rice.

Fonseca-Bermúdez, Ó.J., Giraldo, L., Sierra-Ramírez, R., Moreno-Piraján, J.C., 2023. Removal of hydrogen sulfide from biogas by adsorption and photocatalysis: a review. Environ. Chem. Lett. 21, 1059–1073. https://doi.org/10.1007/s10311-022-01549-z.

Frazier, R.S., Jin, E., Kumar, A., 2015. Life Cycle Assess. Biochar Versus Met. Catal. Use Syngas Clean.62164410.3390/en8010621.

Guo, J., Luo, Y., Lua, A.C., an Chi, R., lin Chen, Y., ting Bao, X., xin Xiang, S., 2007. Adsorption of hydrogen sulphide (H2S) by activated carbons derived from oil-palm shell. Carbon New Y. 45, 330–336. https://doi.org/10.1016/j.carbon.2006.09.016.

Gupta, R.P., Turk, B.S., Portzer, J.W., Cicero, D.C., 2001. Desulfurization of syngas in a transport reactor. Environ. Prog. 20, 187–195. https://doi.org/10.1002/ep.670200315.

Habeeb, O.A., Kanthasamy, R., Ali, G.A.M., Sethupathi, S., Yunus, R.B.M., 2018. Hydrogen sulfide emission sources, regulations, and removal techniques: a review. Rev. Chem. Eng. 34, 837–854. https://doi.org/10.1515/revce-2017-0004.

Heidarinejad, Z., Dehghani, M.H., Heidari, M., Javedan, G., Ali, I., Sillanpää, M., 2020. Methods for preparation and activation of activated carbon: a review. Environ. Chem. Lett. 18, 393–415. https://doi.org/10.1007/s10311-019-00955-0.

Hervy, M., Pham Minh, D., Gérente, C., Weiss-Hortala, E., Nzihou, A., Villot, A., Le Coq, L., 2018. H2S removal from syngas using wastes pyrolysis chars. Chem. Eng. J. 334, 2179–2189. https://doi.org/10.1016/j.cej.2017.11.162.

Ho, J., Yeong, J., Hyeon, M., Sik, Y., Jeong, J., Thoma, G., Hong, Y., 2025. Chemosphere Sustainable removal of gaseous Hg 0 using sulfur functionalized biochar: adsorption experiment and life cycle assessment. Chemosphere 373, 144158. https://doi.org/10.1016/j.chemosphere.2025.144158.

Izhar, T.N.T., Kee, G.Z., Saad, F.N.M., Rahim, S.Z.A., Zakarya, I.A., Besom, M.R.C., Ibad, A, M., 2022. Syafiuddin, Adsorption of hydrogen sulfide (H2s) from municipal solid waste by using biochars. Biointerface Res. Appl. Chem. 12, 8057–8069. https://doi.org/10.33263/BRIAC126.80578069.

Jiang, Q., Li, T., He, Y., Wu, Y., Zhang, J., Jiang, M., 2022. Simultaneous removal of hydrogen sulfide and ammonia in the gas phase: a review. Environ. Chem. Lett. 20, 1403–1419. https://doi.org/10.1007/s10311-021-01366-w.

Khoshnood Motlagh, E., Sharifian, S., Asasian-Kolur, N., 2021. Alkaline activating agents for activation of rice husk biochar and simultaneous bio-silica extraction. Bioresour. Technol. Rep. 16, 100853. https://doi.org/10.1016/j.biteb.2021.100853.

Kim, H.Bin, Kim, J.G., Kim, T., Alessi, D.S., Baek, K., 2021. Interaction of biochar stability and abiotic aging: influences of pyrolysis reaction medium and temperature. Chem. Eng. J. 411, 128441. https://doi.org/10.1016/j.cej.2021.128441.

Kim, Y., Oh, J., Vithanage, M., Park, Y., Lee, J., 2019. Modification of biochar properties using CO 2. Chem. Eng. J. 372, 383–389. https://doi.org/10.1016/j.cej.2019.04.170.

Ko, J.H., Xu, Q., Jang, Y.C., 2015. Emissions and control of hydrogen sulfide at landfills: a review. Crit. Rev. Environ. Sci. Technol. 45, 2043–2083. https://doi.org/10.1080/10643389.2015.1010427.

Lee, J., Yang, X., Cho, S.H., Kim, J.K., Lee, S.S., Tsang, D.C.W., Ok, Y.S., Kwon, E.E., 2017. Pyrolysis process of agricultural waste using CO2 for waste management, energy recovery, and biochar fabrication. Appl. Energy 185, 214–222. https://doi.org/10.1016/j.apenergy.2016.10.092.

Liu, Z., Zhang, F., Liu, H., Ba, F., Yan, S., Hu, J., 2018. Pyrolysis/gasification of pine sawdust biomass briquettes under carbon dioxide atmosphere: study on carbon dioxide reduction (utilization) and biochar briquettes physicochemical properties. Bioresour. Technol. 249, 983–991. https://doi.org/10.1016/j.biortech.2017.11.012.

Marzeddu, S., Cappelli, A., Ambrosio, A., Viotti, P., Boni, M.R., 2021. A Life Cycle Assess. EnergyBiochar Chain Involv. A Gasif. Plant Italy.

Moreira, M.T., Noya, I., Feijoo, G., 2017. Bioresource Technology The prospective use of biochar as adsorption matrix – a review from a lifecycle perspective. Bioresour. Technol. 246, 135–141. https://doi.org/10.1016/j.biortech.2017.08.041.

Nam, H., Wang, S., Jeong, H.R., 2018. TMA and H2S gas removals using metal loaded on rice husk activated carbon for indoor air purification. Fuel 213, 186–194. https://doi.org/10.1016/j.fuel.2017.10.089.

Nguyen, V.T., Nguyen, T.B., Huang, C.P., Chen, C.W., Bui, X.T., Dong, C.Di, 2021. Alkaline modified biochar derived from spent coffee ground for removal of tetracycline from aqueous solutions. J. Water Process Eng. 40, 101908. https://doi.org/10.1016/j.jwpe.2020.101908.

Nowicki, P., Skibiszewska, P., Pietrzak, R., 2014. Hydrogen sulphide removal on carbonaceous adsorbents prepared from coffee industry waste materials. Chem. Eng. J. 248, 208–215. https://doi.org/10.1016/j.cej.2014.03.052.

Pereira, P.H.F., Maia, L.S., da Silva, A.I.C., Silva, B.A.R., Pinhati, F.R., de Oliveira, S.A., Rosa, D.S., Mulinari, D.R., 2024. Prospective life cycle assessment prospective (LCA) of activated carbon production, derived from banana peel waste for methylene blue removal. Adsorption 30, 1081–1101. https://doi.org/10.1007/s10450-024-00485-4.

Premchand, M.Komiyama, Aqsha, Y., 2023. Uemura, a comparative study of oil palm fronds torrefaction under flue gas and nitrogen atmospheres. J. Oil Palm. Res. 35, 75–85. https://doi.org/10.21894/jopr.2022.0027.

Premchand, P., Demichelis, F., Chiaramonti, D., Bensaid, S., Fino, D., 2023. Study on the effects of carbon dioxide atmosphere on the production of biochar derived from slow pyrolysis of organic agro-urban waste. Waste Manag. 172, 308–319. https://doi.org/10.1016/j.wasman.2023.10.035.

Premchand, P., Demichelis, F., Galletti, C., Chiaramonti, D., Bensaid, S., Antunes, E., Fino, D., 2024. Enhancing biochar production: a technical analysis of the combined influence of chemical activation (KOH and NaOH) and pyrolysis atmospheres (N 2 / CO 2) on yields and properties of rice husk-derived biochar. J. Environ. Manage. 370.

Qu, J., Wang, Y., Tian, X., Jiang, Z., Deng, F., Tao, Y., Jiang, Q., 2021. KOH-activated porous biochar with high speci fi c surface area for adsorptive removal of chromium (VI) and naphthalene from water: a ff ecting factors, mechanisms and reusability exploration. J. Hazard. Mater. 401, 123292. https://doi.org/10.1016/j.jhazmat.2020.123292.

Revellame, E.D., Fortela, D.L., Sharp, W., Hernandez, R., Zappi, M.E., 2020. Adsorption kinetic modeling using pseudo-first order and pseudo-second order rate laws: a review. Clean. Eng. Technol. 1, 100032. https://doi.org/10.1016/j.clet.2020.100032.

Sackett, H., 2010. Final Re Port. Statistics 364, 1–93.

Sahota, S., Vijay, V.K., Subbarao, P.M.V., Chandra, R., Ghosh, P., Shah, G., Kapoor, R., Vijay, V., Koutu, V., Thakur, I.S., 2018. Characterization of leaf waste based biochar for cost effective hydrogen sulphide removal from biogas. Bioresour. Technol. 250, 635–641. https://doi.org/10.1016/j.biortech.2017.11.093.

Saleh, T.A., 2018. Simultaneous adsorptive desulfurization of diesel fuel over bimetallic nanoparticles loaded on activated carbon. J. Clean. Prod. 172, 2123–2132. https://doi.org/10.1016/j.jclepro.2017.11.208.

Seo, D., Guo, R., Lee, D., 2021. Perform. Alkaline impregnated biochar Deriv. rice Hull. Hydrog. sulfide Remov. Gas. 26, 0–2.

Shang, G., Liu, L., Chen, P., Shen, G., Li, Q., 2016b. Kinetics and the mass transfer mechanism of hydrogen sulfide removal by biochar derived from rice hull. J. Air

Waste Manag. Assoc. 66, 439–445. https://doi.org/10.1080/10962247.2015.1122670.
Shang, G., Li, Q., Liu, L., Chen, P., Huang, X., 2016a. Adsorption of hydrogen sulfide by biochars derived from pyrolysis of different agricultural/forestry wastes. J. Air Waste Manag. Assoc. 66, 8–16. https://doi.org/10.1080/10962247.2015.1094429.
Shen, Y., Fu, Y., 2018. KOH-activated rice husk char via CO2 pyrolysis for phenol adsorption. Mater. Today Energy 9, 397–405. https://doi.org/10.1016/j.mtener.2018.07.005.
Skerman, A.G., Heubeck, S., Batstone, D.J., Tait, S., 2017. Low-cost filter media for removal of hydrogen sulphide from piggery biogas. Process Saf. Environ. Prot. 105, 117–126. https://doi.org/10.1016/j.psep.2016.11.001.
Surra, E., Costa, M., Bernardo, M., Lapa, N., Esteves, I., Fonseca, I., 2019. New adsorbents from maize cob wastes and anaerobic digestate for H 2 S removal from biogas. Waste Manag. 94, 136–145. https://doi.org/10.1016/j.wasman.2019.05.048.
Thushari, I., Vicheanteab, J., Janjaroen, D., 2020. Material flow analysis and life cycle assessment of solid waste management in urban green areas, Thailand. Sustain. Environ. Res. 30. https://doi.org/10.1186/s42834-020-00057-5.
Tsai, J., 2002. Remov. H. 2 S Exhaust Gas. Use Alkaline Act. Carbon357366.
Voccia, D., Abdel, S., Demichelis, F., Froldi, F., Savorani, F., Tommasi, T., Wachongkum, S., Lamastra, L., 2025. Unlocking the power of Italy ' s bioeconomy: a comparative analysis of immediate vs. deferred impact on energy generation through straw valorisation, 380.
Wang, H., Larson, R.A., Runge, T., 2019b. Impacts to hydrogen sulfide concentrations in biogas when poplar wood chips, steam treated wood chips, and biochar are added to manure-based anaerobic digestion systems. Bioresour. Technol. Rep. 7, 100232. https://doi.org/10.1016/j.biteb.2019.100232.
Wang, S., Lee, Y.N., Nam, H., Nam, H., Kim, H.K., 2019a. Chemical activation of porous diatomite ceramic filter for the adsorption of TMA, H2S, CH3COOH and NH3: isotherm and kinetic studies. J. Environ. Chem. Eng. 7, 103481. https://doi.org/10.1016/j.jece.2019.103481.
Wani, I., Sharma, A., Kushvaha, V., Madhushri, P., Peng, L., 2020. Effect of pH, volatile content, and pyrolysis conditions on surface area and O/C and H/C ratios of biochar: towards understanding performance of biochar using simplified approach. J. Hazard. Toxic. Radioact. Waste 24, 1–11. https://doi.org/10.1061/(asce)hz.2153-5515.0000545.
Xu, X., Cao, X., Zhao, L., Sun, T., 2014. Comparison of sewage sludge- and pig manure-derived biochars for hydrogen sulfide removal. Chemosphere 111, 296–303. https://doi.org/10.1016/j.chemosphere.2014.04.014.
Yan, R., Chin, T., 2004. Influ. Surf. Prop. Mech. H. 2 S Remov. Alkaline Act. Carbons 38, 316–323.
Yi, Z., Li, C., Li, Q., Zhang, L., Zhang, S., Wang, S., Qin, L., Hu, X., 2022. Influence of CO2 atmosphere on property of biochar from pyrolysis of cellulose. J. Environ. Chem. Eng. 10, 107339. https://doi.org/10.1016/j.jece.2022.107339.
Yuan, Y., Huang, L., Zhang, T.C., Ouyang, L., Yuan, S., 2021. One-step synthesis of ZnFe2O4-loaded biochar derived from leftover rice for high-performance H2S removal. Sep. Purif. Technol. 279, 119686. https://doi.org/10.1016/j.seppur.2021.119686.
Zhao, J., Ye, Z.L., Pan, X., Cai, G., Wang, J., 2022. Screening the functions of modified rice straw biochar for adsorbing manganese from drinking water. RSC Adv. 12, 15222–15230. https://doi.org/10.1039/d2ra01720b.
Zhao, Y., Monteagudo, J., 2026. CO 2 capture by olive pomace biochar: effect of relative humidity, isosteric heat of adsorption, and a preliminary life cycle assessment investigation, 385. https://doi.org/10.1016/j.seppur.2025.136445.
Zulkefli, N.N., Shahbudin, M., Id, M., Nor, W., Wan, R., Jahim, J., Rejab, S.A., Lye, C.C., 2019. Removal of hydrogen sulfide from a biogas mimic by using impregnated activated carbon adsorbent. PLoS One 2–5.